Mediterranean Low-Pressure Systems in Radio Occultation Data

Master Thesis

to obtain the academic degree
Master of Science

Stephanie Haas BSc
January 2020

Supervisor
Assoc. Prof. Mag. Dr. Ulrich Foelsche
University of Graz, Austria

Co-supervisor
Mag. Dr. Julia Danzer
University of Graz, Austria

Institute for Geophysics, Astrophysics, and
Meteorology/Institute of Physics (IGAM/IP)
Wegener Center for Climate and Global Change

Contents

Acknowledgements

Many people have supported me during my studies over the last few years. Whether it was academically with their expertise, personally with advice and comfort, or helping me to focus on something else for a while in my sports clubs. I can't name all of those who accompanied me through this process, but be assured, that I appreciate Your help very much and that I'm glad to experience so much support on a daily basis.

First of all I want to thank my supervisor Ulrich Foelsche who awoke my interest in climate physics in the first place and provided me with the topic for my thesis. He also supported me with his knowledge and introduced me to my co-supervisor Julia Danzer. No matter how busy they were, I could always just walk upstairs, knock on their doors and ask for help. Julia, I want to thank You for the time You spent checking my code, getting data I needed, and giving feedback on my thesis. I really enjoyed working with both of You and hope that we will be able to do so again in the future.
I also want to thank the whole team at the Wegener Center under the leadership of Andrea Steiner, who I want to thank for the research funding I received. Thank You all for Your expertise and for all the resources I could use there.

My parents and my brother deserve a special thank you. They always support me in every way one can think of and show me how proud they are of me. Thank you for that and everything else You have done for me.
To all my friends (especially from my sports clubs), thank you for the time we spend together improving a kata or working on my yeopchagi. Thanks for helping me keep my mind of academic things for a couple of hours each week.
Last but not least, I sincerely want to thank my boyfriend Daniel. He is my companion since early on in my studies and always supports me, no matter what. He always believes in me and encourages me to go beyond the limits I imagine myself being in. Without him this thesis would not have been possible.

Abstract

Mediterranean low-pressure systems have a strong influence on Austrian weather. Especially in autumn, heavy precipitation events are caused by Mediterranean low-pressure systems which accumulate south of the Alps. Floods or extreme amounts of snow are often the results of such events and lead to severe damage on, e.g., streets and buildings. Since Mediterranean low-pressure systems play such an important role in the formation of the Austrian weather, it is desirable to know as much as possible about this phenomenon. Including many different sources of data helps expanding our knowledge of Mediterranean low-pressure systems and their behavior, which can lead to improvements in the detection and prediction of such systems.

The satellite-based Global Positioning System (GPS) Radio Occultation (RO) with its all-weather capability and global coverage can be used to retrieve profiles of humidity. While its independence of weather makes it a very promising method for investigating low-pressure systems, the sparse horizontal resolution of RO measurements makes it quite difficult to detect and analyze local low-pressure systems which are usually smaller than the horizontal resolution of the RO method (300 km). Nevertheless, out of scientific interest, and with keeping the high impact of Mediterranean lows on the Austrian weather in mind, the detectability of low-pressure systems in RO data is worth investigating.

The aim of this work is to assess whether Mediterranean low-pressure systems, which lead to severe precipitation events in Austria, can be detected in RO obtained humidity data. This is achieved by investigating the amount of precipitable water and the specific humidity for well-known precipitation events in the years 2009, 2010, 2013, and 2014. Furthermore, the results from the RO data are compared to reanalyses and forecasts from the European Centre for Medium-range Weather Forecast (ECMWF) to investigate their advantages and disadvantages.

While the selected precipitation events can be seen in the RO derived data, due to too strong averaging, the used data weren't ideal for the posed question. In that case it seems, that the method exhibits no significant advantages in comparison to the data of the ECMWF reanalysis. It can be used as an additional source for well-established low-pressure system detecting methods but shouldn't be used for that purpose on its own without ancillary data and information. Nevertheless, even though the used data weren't ideal for the posed question, all the selected events can be seen in the data, which makes it a promising topic for future studies.

Zusammenfassung

Mediterrane Tiefdrucksysteme haben einen großen Einfluss auf das Wetter in Österreich. Besonders im Herbst, werden häufig starke Niederschlagsereignisse von südlich der Alpen angestauten mediterranen Tiefdrucksystemen verursacht. Überschwemmungen und Starkschneefälle sind oft die Folge. Nachdem mediterrane Tiefdrucksysteme eine derart wichtige Rolle in der Entstehung des österreichischen Wetters spielen, ist es wichtig so viel wie möglich über diese Formationen zu wissen. Je mehr unterschiedliche Datenquellen für diesen Zweck genutzt werden können, desto besser wird das Verständnis über mediterrane Tiefdrucksysteme und deren Verhalten, was zu einer Verbesserung in der Erkennung und der Vorhersage solcher Systeme führen kann.

Die satellitenbasierte Global Positioning System (GPS) Radio Okkultations (RO) Methode kann durch ihre Wetterunabhängigkeit dazu genutzt werden Feuchtigkeitsprofile zu erfassen. Obwohl die Wetterunabhängigkeit und die globale Abdeckung der Methode diese sehr geeignet erscheinen lassen Tiefdrucksysteme zu untersuchen, so macht es die geringe horizontale Auflösung von RO Messungen schwierig derartige Systeme zu untersuchen, da diese meistens eine deutlich geringere räumliche Ausdehnung haben. Wissenschaftliche Neugier und der große Einfluss von mediterranen Tiefdrucksystem auf das österreichische Wetter hingegen, sind Motivation genug, um Tiefdrucksysteme in RO Daten zu untersuchen.

Das Ziel dieser Arbeit ist es zu überprüfen ob mediterrane Tiefdrucksysteme, welche zu Starkniederschlagsereignissen in Österreich geführt haben, in von RO abgeleiteten Feuchtigkeitsprofilen detektiert werden können. Hierzu wird die Menge des ausfällbaren Niederschlagswassers und der spezifischen Feuchte für bekannte Niederschlagsereignisse in den Jahren 2009, 2010, 2013 und 2014 untersucht. Außerdem werden die Ergebnisse der RO Daten mit Analysen und Vorhersagen des European Centre for Medium.range Weather Forecast (ECMWF) verglichen, um mögliche Vor-/Nachteile der RO Methode zu untersuchen.

Die ausgewählten Niederschlagsereignisse können zwar in den RO Daten detektiert werden aber die starke Mittelung der verwendeten Daten und das Fehlen von bodennahen Messungen war nicht ideal für die gestellte Frage. Demnach scheint die Detektion von mediterranen Tiefdrucksystemen mittels RO Feuchtigkeitsdaten keine signifikanten Vorteile gegenüber der ECMWF Analyse zu haben. Während die Methode als zusätzliche Informationsquelle für bereits bestehende Detektionsmethoden genutzt werden kann, so sollte sie nicht allein ohne zusätzliche Daten

für diesen Zweck eingesetzt werden. Nichtsdestotrotz, obwohl die verwendeten Daten nicht ideal waren, kann man alle Niederschlagsereignisse in den Daten sehen, was die Methode vielversprechend für zukünftige Studien mit einem Fokus auf der vertikalen Struktur von Tiefdrucksystemen macht, worin die hohe vertikale Auflösung der RO Methode zu neuen Erkenntnissen in diesem Gebiet führen kann.

Introduction

Mediterranean low-pressure systems have a strong influence on Austrian weather. Especially in autumn, heavy precipitation events with daily precipitation amounts of more than 200 mm are not unusual for the western Mediterranean. Reliefs, such as the Alps or the Massif Central, slow down frontal disturbances and strengthen them even more. Floods or extreme amounts of snow are the results of such events and lead to severe damage in Central Europe and therefore also in Austria. Despite having such a huge influence on the Central European weather, the Mediterranean is also one of the hot spots of climate change. Which means that the climate in this region is especially sensitive towards global change. While it is expected that the mean precipitation will decrease drastically, the precipitation variability during (warm) seasons will increase. This, in combination with a temperature increase of 4.4 °C, will affect the formation and behavior of low-pressure systems in the Mediterranean and therefore our every day weather and life (HyMeX 2019). Since Mediterranean low-pressure systems play such an important role in the formation of the Austrian weather, it is desirable to know as much as possible about this phenomenon. Including many different sources of data helps expanding our knowledge of Mediterranean low-pressure systems and their behavior, which can lead to improvements in the detection and prediction of such events.

The satellite-based Global Positioning System (GPS) Radio Occultation (RO) method has already been applied in multiple different atmospheric studies to retrieve profiles of, e.g., temperature (Feltz et al. 2014). The data obtained by this method is also used in numerical weather prediction (Poli 2006), vertical climate monitoring (Foelsche et al. 2006), in climate change studies (Löscher and Kirchengast 2006), and in humidity studies (Rieckh et al. 2017). The RO method has numerous advantages such as, global coverage, high vertical resolution, and all weather capability. The independence of weather is a desirable feature for the observation of low-pressure systems. Nevertheless, the quality of humidity profiles derived from RO measurements is still in need of improvement. While the vertical resolution of the RO method is very high, its horizontal resolution is quite sparse. In the lower and mid troposphere, the uncertainty of RO measurements is high, which makes investigating low-pressure systems in terms of humidity more difficult (Kursinski et al. 1997). Despite the comparatively low quality of RO derived humidity data and its low horizontal resolution, scientific interest and the importance of Mediterranean lows for the Austrian weather, are motivations to investigate the detectability of Mediterranean low-pressure systems in RO data.

The aim of this work is to assess whether Mediterranean low-pressure systems can be detected in RO obtained humidity data. This is achieved by calculating the amount of precipitable water above Europe for well known precipitation events and comparing them to weather maps, as well as to reanalyses and forecasts from the European Centre for Medium-range Weather Forecast (ECMWF). The comparison to ECMWF data is also used as an indicator for possible advantages and disadvantages of the RO obtained humidity data. In order to get a more comprehensive understanding of these low-pressure systems, the vertical structure of the humidity data up to 500 hPa is also investigated and compared to the ECMWF data.

The thesis is structured as follows: Part 1 describes the theoretical background of the thesis and gives a short introduction into the Earth's Atmosphere, Atmospheric Circulation, and the Radio Occultation Method. Part 2 gives information about the data used in the work. It also describes the examined precipitation events and the methodology of the thesis. In Part 3 the results of the thesis are presented and discussed.

Part I.

Theoretical Background

1. The Earth's Atmosphere

1.1. Atmospheric Structure

There are multiple parameters which can be used to distinguish different atmospheric layers. Using a distinction by temperature, the atmosphere can be divided into four layers: troposphere, stratosphere, mesosphere, and thermosphere. One can also define the exosphere, which forms the outermost layer of Earth's atmosphere and has no distinct boundary towards outer space.

- The **troposphere** reaches from the Earth's surface up to about 12 km. Water in every form plays a very important role in this layer and basically all weather phenomena occur in the troposphere. The temperature in the troposphere decreases by 6-10 K per km, which is due to the fact that this layer gets mainly heated by the surface. This also dominates the (thermo-)dynamics of the troposphere besides Earth rotation. About 80% of the atmosphere's mass is concentrated in this area.
- Between about 8 km (above the poles) and 18 km (above the equator) the **stratosphere** starts, which ranges up to 50 km. In contrast to the troposphere, the stratosphere is very dry. It is not very well vertically mixed and contains the ozone layer which is the reason for the temperature increase with height in this region. The bad vertical mixing results in a very stable layering.
- The **mesosphere** extends from 50 km to about 80 km above the Earth's surface. In this layer the temperature decreases with height whereby the density doesn't decrease as much with height as before. This is the reason why most meteors burn up in this layer. The temperature decrease is a result of radiative emission from CO_2.
- The last layer, not including the exosphere, is the **thermosphere**. In the thermosphere the temperature increases again with height but it shows significant differences between day and night, as does the density. This layer reaches up to about 700 km.

Another way to distinguish different atmospheric layers is via homogenity. Up until about 100 km the atmosphere is well mixed, this is the so-called homosphere which includes the troposphere, the stratosphere, the mesosphere and the lower part of the thermosphere. Above the homosphere is the heterosphere, where the

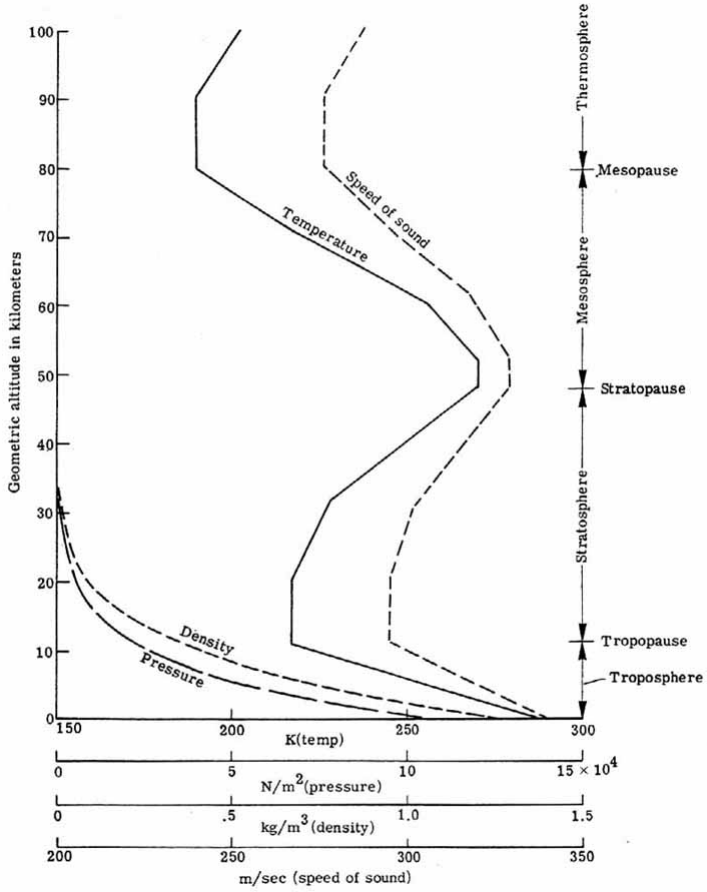

Figure 1.1.: Structure of Earth's Atmosphere and Gradients of different parameters (NASA 2013)

chemical composition varies with height. The percentage of heavy gases is higher at the bottom of the heterosphere and decreases with height, whereas the percentage of light gases increases with height.
The Earth's atmosphere can also be divided by the influence of the magnetic field into the dynamo layer and the magnetosphere. A distinction by electron density divides the atmosphere into the neutral atmosphere and the ionosphere (Kertz 1971; Brunner 2014). Figure 1.1 shows the gradients of temperature, pressure, density, and speed of sound throughout the atmosphere.

1.2. The Troposphere

The troposphere got its name from the Greek word *tropos* which means motion, it is therefore "the layer in motion". According to Brönnimann (2018), one can divide the troposphere into:

- The **planetary boundary layer** is the lowest part of the atmosphere which reaches up to about 1.5 km. The Earth's surface has a stong influence on the planetary boundary layer through mechanical and thermal processes.
- The **free troposphere**, which is directly above the planetary boundary layer, isn't directly influenced by the Earth's surface. It is the layer where most of the weather phenomena occur.
- The **tropopause** is the boundary layer towards the stratosphere. It is the coldest region of Earth's atmosphere.

As mentioned before, water plays a very important role in the troposphere. It not only contains about 80% of the atmospheric mass but also 99% of the total mass of water vapor and aerosols. (McGraw-Hill 1984) 50% of the atmospheric water vapor are found below 2 km altitude (Rieckh 2018). The atmospheric water vapor, which is a result of the process of evaporation, makes the troposphere the wettest of all atmospheric layers. The water vapor mixing ratios of the higher layers are all up to four orders of magnitude smaller than the one of the troposphere (Dowling and Showman 2007). That means the water vapor content decreases with height, as does the temperature, the pressure and the density in the troposphere (Atmospheric Research 2019b). The decrease in temperature with height can be traced back to the main heat source of the troposphere, which is the Earth's surface. The resulting heat transfer leads to a good vertical mixing. The top of the atmosphere is marked by an inversion layer - the tropopause (Dowling and Showman 2007). The temperature reaches a minimum of about -50 °C in the tropopause, from here on up the temperature increases again (Roedel 1994). The decrease of pressure with height also depends on the temperature. Equation 1.1 gives the pressure change in a vertical air column with a standard cross section.

$$dp = -\rho \cdot g \cdot dz\,, \tag{1.1}$$

where dp is the pressure change, ρ the density, g the acceleration due to gravity and dz an infinitesimal small height. The ideal gas law $pV = nRT$ and equation 1.2 lead to equation 1.3.

$$\rho = \frac{M}{V} = \frac{Mp}{RT}\,, \tag{1.2}$$

$$dp = -p \cdot \frac{Mg}{RT} \cdot dz\,, \tag{1.3}$$

T denotes the absolute temperature and is assumed constant (as is g), R is the universal gas constant ($R = 8.315\ \mathrm{J\,mol^{-1}\,K^{-1}}$), M the molar mass and V the molar volume. Integration leads to:

$$p = p_0 \cdot exp\left(-\frac{Mg}{RT} \cdot z\right)\,, \tag{1.4}$$

Component	Molar Mass [g mol^{-1}]	Volume-%	Mass-%
Nitrogen N_2	28.02	78.09	75.73
Oxygen O_2	32.00	20.95	23.14
Argon Ar	39.94	0.93	1.28
CO_2	44.01	0.04	0.051
Neon Ne	20.18	18.2×10^{-4}	10.5×10^{-4}
Helium He	4.003	5.24×10^{-4}	0.724×10^{-4}
Krypton Kr	83.8	1.14×10^{-4}	3.3×10^{-4}
Xenon Xe	131.3	0.087×10^{-4}	0.39×10^{-4}

Table 1.1.: Components of the dry Atmosphere, taken and translated from: Roedel (1994). Amended with the values for CO_2 from: Engineering ToolBox (2003).

with the surface pressure p_0. Equation 1.4 shows that the pressure decreases faster with height, when the temperature is low (Roedel 1994).

1.3. Atmospheric Composition

The composition of the atmosphere varies with height. Within the very well mixed homosphere, however, the composition is practically constant over time and space. The main components of the homosphere are listed in table 1.1. Figure 1.2 illustrates the (volume) percentages of the different components (Roedel 1994). The percentage of water vapor in the atmosphere varies strongly, while it can reach up to 5% in surface near regions it is very scarce higher up. As a result, mixing ratios are always given with respect to dry air (Brunner 2014).

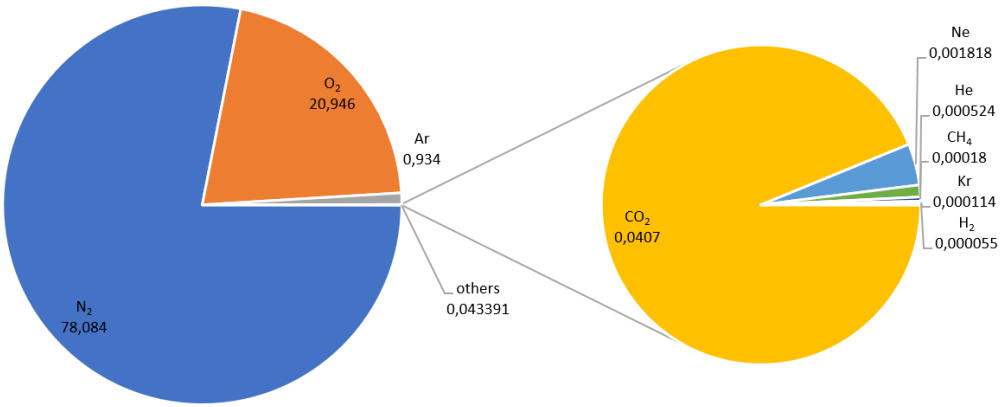

Figure 1.2.: Volume-% of the atmosphere's components (SJH 2019)

As shown above, the atmosphere consists mainly of nitrogen and oxygen. This has not always been the case. The original atmosphere of the Earth consisted of hydrogen, helium, methane and ammonia. Since these gases all got lost to space, a new atmosphere out of water vapor, CO_2, and H_2S arose. The amount of oxygen increased slowly over time but it couldn't accumulate at first. This was only possible after the atmosphere and the Earth's surface were completely oxidated. The amount of nitrogen in the atmosphere origins from volcanic eruptions, e.g., which could accumulate very well, since nitrogen hardly reacts in the atmosphere. Even though the composition of the atmosphere changed in the past, it can be considered constant on climatic time scales (Brönnimann 2018).

1.4. Water Vapor in the Atmosphere

Even tough water only accounts for 0.25% of the atmospheric mass, it plays a very important role in determining the properties of the atmosphere and hence our every day live. The amount of water in the atmosphere would form a liquid layer of only 2.5 cm depth around the Earth (the oceans would form a layer of 2.8 km thickness). 99.5% of this atmospheric water is distributed in the form of vapor and determines for example the partition of the Sun's energy. Despite the comparatively small amounts of water in the atmosphere, it is the most abundant liquid on Earth. Even though water vapor also magnifies the effects of climate change driving agents, it cannot drive climate change itself because of its strong coupling to surface temperature. Some of its properties are listed below (Stevens and Bony 2013; Rieckh 2018).

- **Bent Molecular Structure:** The oxygen atom has six valence electrons and therefore needs another two to fill up its outer shell. The oxygen atom shares these two electrons with the hydrogen atoms, which leads to two unbonded electron pairs. The hydrogen atoms are as far away from the lone electron pairs as possible, which results in a bending angle of 104.5° (Elmhurst College - Charles E.Ophardt 2003).
- **Latent Heat:** Water has with 4.1814 $\mathrm{J\,kg^{-1}\,K^{-1}}$ the second highest specific heat capacity of all heteroatomic molecules. Additionally it has a high enthalpy of vaporization of 40.65 $\mathrm{kJ\,mol^{-1}}$. Both of these high values can be explained by the bent molecular structure of the H_2O molecule. These properties moderate Earth's climate since they buffer large temperature fluctuations.
- **Triple Point:** The triple point of any substance describes the temperature and pressure where all three states (solid, liquid, gaseous) can exist in equilibrium. For water the triple point lies at a temperature of 0.01 °C and a pressure of 607.9 Pa (American Meteorological Society 2012). Both of these values lie within normal atmospheric conditions which makes water occur in all three forms in the atmosphere.

- **Electromagnetic Absorption:** Water absorbs most of ultraviolet (UV), infrared (IR) and microwave (MW) light. The absorptions in the MW and far IR are due to rotational transitions, while absorption in the mid and near IR are due to vibrational transitions. The weak absorption in the red part of the visible spectrum leads to water's blue color. Figure 1.3 shows the absorption spectrum of water vapor.

- **Electronegativity:** The electronegativity of oxygen (3.44) is higher than the one of hydrogen (2.2). That leads to a dipole moment between each of the H atoms and the O atom in the water molecule. In combination with the bent structure of the H_2O atom the O atom is partially negative while the H atoms are partially positive, in other words: a permanent dipole moment exists (Campbell and Farrell 2009).

- **Greenhouse Gas:** Water vapor is the most abundant greenhouse gas in the atmosphere. It plays an important role in feedback loops which regulate our climate. For example: a warmer atmosphere leads to more evaporation of water from the surface and therefore a higher concentration of water vapor in the atmosphere. The higher air temperature allows for higher humidity values (according to the Clausius-Clapeyron-Equation) and increases the water vapor concentration even more. Since water is a greenhouse gas it absorbs thermal IR energy which heats the atmosphere and the loop starts once again. However the importance of this positive feedback loop is not yet clearified. A higher water vapor concentration in the atmosphere also leads to more clouds, which increase the albedo and therefore protect the Earth from incoming IR radiation (National Oceanic and Atmospheric Administration 2019).

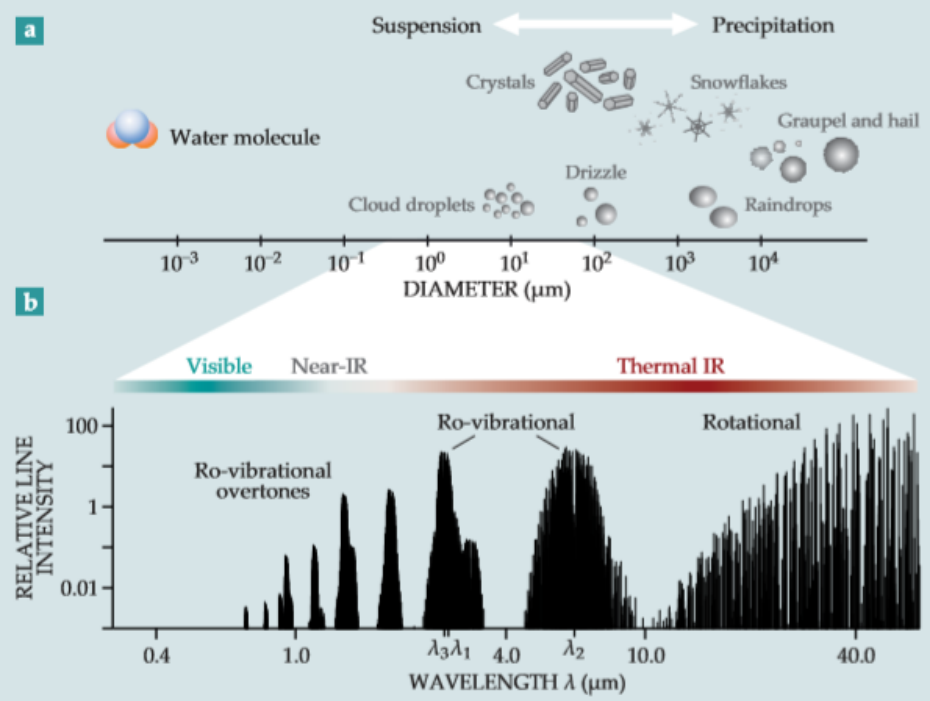

Figure 1.3.: Hydrometeors (a): the condensed forms of water in the atmosphere come in several sizes and shapes. (b) The near- and thermal infrared regions of the spectrum excite the water molecule and produce its rotational-vibrational (or ro-vibrational) and rotational bands. Specific lines λ_1, λ_2, and λ_3 mark the symmetric stretching mode, bending mode, and asymmetric stretching mode, respectively. Figure and caption taken from (Stevens and Bony 2013).

Parameters of Water Vapor

The most important parameters in connection with humidity, as described in Roedel (1994) and Brönnimann (2018), are listed below:

Absolute Humidity ρ_w

The absolute humidity describes the concentration of water vapor as water mass per air volume. It therefore describes a density and is given in $\mathrm{kg\,m^{-3}}$.

$$\rho_w = \frac{m_w}{V_{tot}}\,, \tag{1.5}$$

with m_w being the mass of the water vapor within the air parcel and V_{tot} being the total volume of the moist air. One can also express the absolute humidity via rearranging the ideal gas law:

$$\rho_w = \frac{e}{R_w \cdot T}\,, \tag{1.6}$$

where e describes the vapor pressure (see section 1.4), R_w the gas constant of water ($R_w = 461.52\ \mathrm{J\,kg^{-1}\,K^{-1}}$) and T the absolute temperature.

Mixing Ratio r

The mixing ratio describes the mass of water in the air. It is calculated as the ratio of the mass of water m_w to the mass of dry air m_{dry},

$$r = \frac{m_w}{m_{dry}} = \frac{0.622 \cdot e}{p - e}\,. \tag{1.7}$$

Specific Humidity q

The specific humidity is nearly identical to the mixing ratio but it describes the ratio of mass of water to the total air mass. It can be calculated via:

$$q = \frac{m_w}{m} = \frac{m_w}{m_{dry} + m_w} = \frac{r}{r+1} = \frac{0.622 \cdot e}{p - 0.378 \cdot e}\,, \tag{1.8}$$

with the mass of water m_w, the total air mass m, the mass of dry air m_{dry}, the mixing ratio r (see section 1.4) and the pressure p. The specific humidity is usually given in $\mathrm{g\,kg^{-1}}$. Specific humidity q and absolute humidity ρ_w are linked via:

$$q = \frac{\rho_w}{\rho}\,, \tag{1.9}$$

with the density of water ρ.

Water Vapor Pressure e

e describes the partial pressure of water vapor in the atmosphere. It can be derived via:

$$e = \frac{q \cdot p}{0.622 + 0.378q} \,. \tag{1.10}$$

Above a flat water surface, water vapor condenses if it reaches the saturation vapor pressure e_s. At this point, the same amount of particles change from the gaseous state to the liquid state as from the liquid state to the gaseous state. The water vapor pressure is usually given in hPa. A change of e_s depends on the specific vaporization enthalpy L_v and on the temperature T, as described by equation 1.11, the Clausius-Clapeyron-Equation (Brönnimann 2018):

$$\frac{de_s}{e_s} = \frac{L_v}{R_w T^2} dT \,. \tag{1.11}$$

Relative Humidity RH

The relative humidity is usually given in percent. It describes the ratio of water vapor pressure e to the saturation vapor pressure e_s,

$$RH = \frac{e}{e_s} \cdot 100\% \,. \tag{1.12}$$

Precipitable Water PW and Integrated Water Vapor IWV

The parameters PW and IWV are especially relevant for this work. The PW, usually given in mm, describes how high a water column above a unit area would be, if all the water in that column was precipitated as rain. The IWV gives the mass of water vapor per unit area. The relationship between these parameters is therefore given as:

$$PW = \frac{IWV}{\rho_l} \,, \tag{1.13}$$

with ρ_l being the density of liquid water, which is about 1 $\mathrm{g\,cm^{-3}}$. The IWV is obtained via,

$$IWV = \int_0^\infty \rho_w dz \,. \tag{1.14}$$

2. Atmospheric Circulation

2.1. Global Circulation

As shown in figure 2.1, Earth's atmospheric circulation can be divided into different regions:

- Up to 30-35° N (or S) are the **Trade Wind Zones**. The trade winds are relatively consistent winds from northeast (southeast on the southern hemisphere). Warm moist air rises in the zones of high solar radiation and forces air to flow back on the surface. Due to the Coriolis force the trade winds get deflected westward. The inward flow on the surface is called convergence, while the outward flow higher up in the atmosphere describes a divergence.
- The **Innertropical Convergence Zone (ITCZ)** describes the area where the trade winds of the northern hemisphere meet the ones of the southern hemisphere. The air pressure in the ITCZ is relatively low and rises with latitude.
- From 35° to 70° N (or S) lie the so-called **Westerlies**. The winds in these zones are mainly due to the temperature decrease from the tropics towards the poles. Wave movements and circulation also have an impact on the formation of these winds. Characteristic for the westerlies are waves with different wave length, high/low pressure systems and fronts.
- From the westerlies up to the **Poles** the pressure increases slightly. These areas are dominated by katabatic winds (fall winds) that get deflected eastward due to the coriolis force.

(Brönnimann 2018)
Since this work focuses on low pressure systems in the mediterranean, the westerlies on the northern hemisphere is the zone of interest in this thesis.

The Westerlies

The westerlies got their name from the westward winds that are very common in these zones. But the weather in these areas shows that west winds are not the only winds in the westerlies. The general wave movement in the westerlies forms a wave pattern with 3-5 waves around the Earth. These waves tend to form at the same places and have a velocity that is nearly constant which is characterized by the

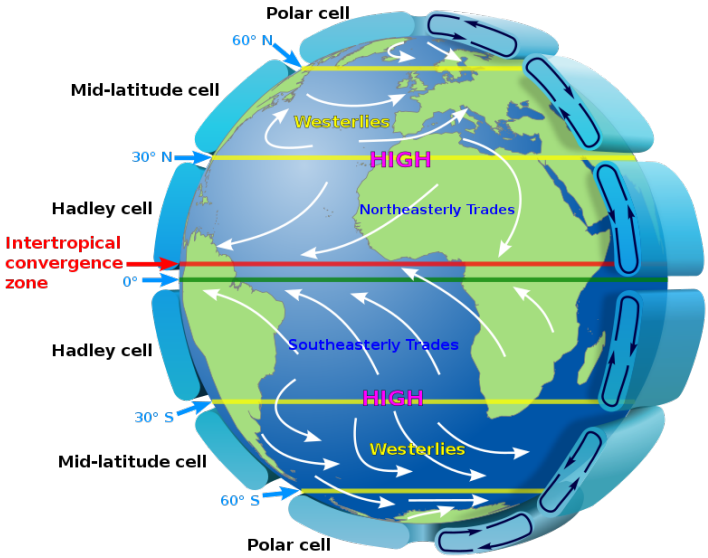

Figure 2.1.: Large scale atmospheric circulation on Earth (Kaidor 2013)

flow at a height of 5-6 km (about 600-500 hPa). At this height level the air density only depends on pressure, it is barotropic. The niveaus above and below that height are baroclinic, which means that surfaces of equal pressure (isobars) are not parallel to surfaces of equal temperature (isotherms). This leads to a pressure gradient on the isotherms, an important feature in the formation of cyclones. The general wave movement of the westerlies is therefore defined by barotropic waves (Rossby-waves) and baroclinic waves (Roedel 1994; Brönnimann 2018).

2.2. Low Pressure Systems

Winds that circulate around an area of low pressure on the Earth's surface are called low pressure systems. These so-called cyclones usually appear in combination with rain or snow. Due to the coriolis force, this flow moves counterclockwise on the northern hemisphere and clockwise on the southern hemisphere. Since the Coriolis force plays an important role in the formation of cyclones, cyclones can move essentially everywhere on Earth, except for the equatorial belt. The characteristics of cyclones differ significantly depending on the hemisphere they appear on. On the southern hemisphere they are uniformly distributed and usually formed in regions between 30° and 40° S. The cyclones move southeasterly and reach their maximum at about 60° S. On the northern hemisphere land masses and mountains obstruct such a path. The cyclones therefore describe different tracks, usually above the oceans (Encyclopædia Britannica 2016b; Brönnimann 2018).

In order for cyclones to develop it is necessary that a baroclinic instability in the general wave movement occurs. Within a baroclinic wave a rather weak

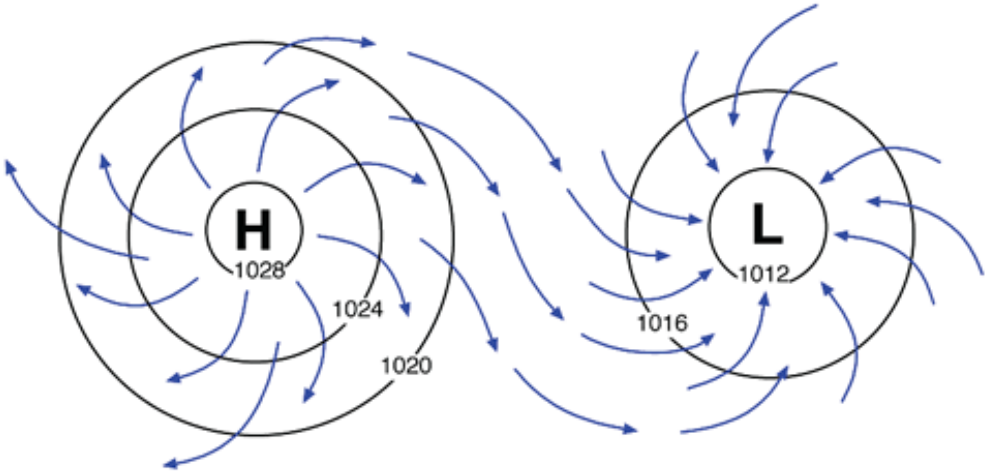

Figure 2.2.: Flow around High/Low Pressure Systems on the Northern Hemisphere (Midwestern Regional Climate Center 2016)

convergence near the surface and a quite strong divergence higher up can be found in the branch which points towards the pole. This leads to a vertical movement and to a decrease in pressure, since more air is moving outwards than inwards. The decreasing pressure triggers a cyclonic movement around the area. The exact opposite happens in the branch that points to the equator. This leads to additional flows towards the pole/equator in the corresponding branches. The amplitude of the general wave movement increases, which also increases the convergences and divergences. Since the additional flows were induced by the convergences and divergences in the first place, they get stronger too. This makes the general wave unstable and enables the development of huge pressure differences (Roedel 1994). There are 3 stages of cyclogenesis:

1. Start: Due to an initial disturbance a wave is formed wherein warm air flows northward and cold air southward. The pressure on the surface decreases and the amplitude of the general wave amplifies as described before.

2. Peak of development: Cold fronts travel faster than warm fronts which leads to a narrowing of the warm front until it gets detached from the Earth's surface.

3. Fully grown cyclone: The cold air catches up with the warm air and the warm air already got detached from the surface. In the summer the withdrawing cold air is warmer than the advancing cold air, which shows the characteristics of a cold front in surface near regions. This is exactly the other way around in winter, therefore the resulting formation has the characteristics of a weak warm front near the surface.

It usually takes 1-2 days from the first disturbance to the fully grown cyclone (Roedel 1994). The dimensions of a cyclone depend on its origins: tropical cyclones have

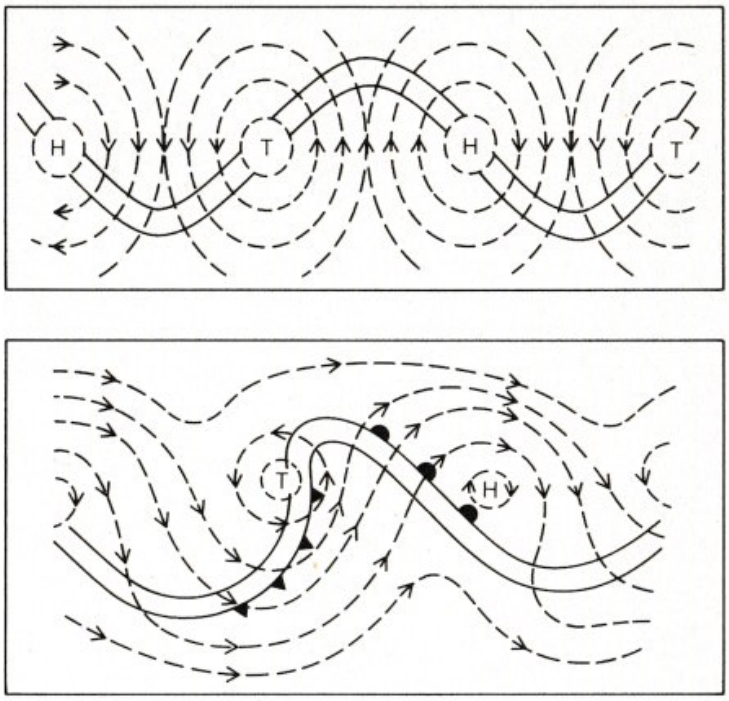

Figure 2.3.: Schematic flow (dashed line) and wave front (solid line) in a baroclinic wave. Top: In the frame of reference of the wave. Bottom: In the space fixed system under additional consideration of the underlying easterly flow. Triangles mark cold fronts, semi circles warm fronts, H are high pressure systems and T low pressure systems (after the German word for Lows: "Tief"). Figure and caption taken and translated from Roedel (1994).

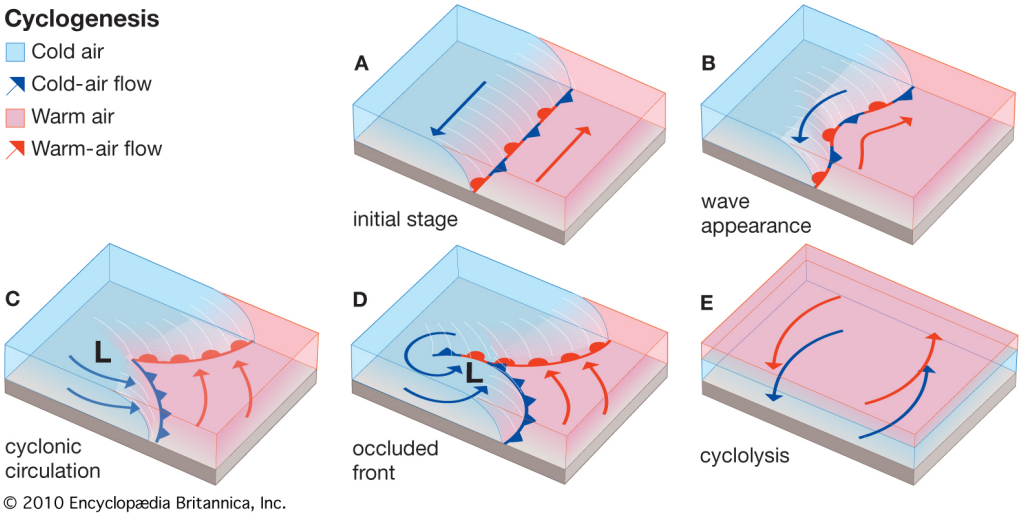

Figure 2.4.: Evolution of a wave (frontal) cyclone (Encyclopædia Britannica 2016a).

a diameter of 100-1000 km while extratropical cyclones are much bigger with a diameter of 1000-4000 km (Encyclopædia Britannica 2016b).

Mediterranean Low Pressure Systems

The Mediterranean sea has a high influence on the formation of cyclones in this region. It is not only a source of energy but also delivers the necessary moisture for cyclogenesis and influences the tracks of the cyclones with its complex land topography. On average there are about 55 cyclones with a lifetime of more than 12h in the Mediterranean each month. The cyclones are either formed directly above the sea or get reinforced during their track over it. In contrast to other low pressure systems, the Mediterranean cyclones only have an average lifetime of about 28h and are also smaller than cyclones in, e.g., the North Atlantic. The size of the cyclones influences their lifetimes, bigger systems live longer than smaller ones. According to Trigo et al. (1999) there are 7 different regions in the Mediterranean where cyclones are formed:

1. The **Genoa** centre, where cyclones are formed in the Lee of the Alps. These Cyclones often move over North-Italy along the eastern Alps further north and are the cause of severe precipitation events in these regions (Deutscher Wetterdienst 2019).

2. **Sahara** cyclones mostly occur in the Mediterranean spring from March to June.

3. **Relatively warm land** which leads to a sea-land contrast dominates the cyclogenesis on the Iberian peninsula from June to August.

4. From the **Aegean Sea** cyclones origin mainly in winter and spring (October to June).
5. Eastern Black Sea
6. Cyprus
7. Middle East (since this region lies at the edge of the Mediterranean its influence is probably overestimated).

Especially in autumn Mediterranean low pressure systems cause heavy precipitation events south of the Alps. These systems arise if cold air from northern europe advances very far south, where it meets the still warm air above the Mediterranean. This leads to precipitation areas that accumulate south of the alps (ZAMG 2014a).

3. Radio Occultation

The satellite-based Global Positioning System (GPS) Radio Occultation (RO) is a remote sensing technique for sounding atmospheres of planets, developed at Stanford University and NASA's Jet Propulsion Laboratory (JPL) (Kursinski et al. 1997; Danish Meteorological Institute 2019). Since 1995 the technique is not only applied to planetary atmospheres but also to Earth's atmosphere (Hajj et al. 2002). At present there are 31 operational GPS satellites in medium-earth orbits (MEO) at an altitude of 20,200 km (NOAA 2019). The inclination of these circular orbits is about 55°, with a period of 12h. These satellites enable a global coverage of atmospheric parameter profiles such as refractivity, temperature, pressure and water vapor (Kursinski et al. 1997). The RO technique is based on GPS phase delay measurements by a receiver in a low-earth orbit (LEO) which is tracking a GPS satellite that rises/sets behind the Earth's atmosphere's limb (Fig. 3.1) (Hajj et al. 2002). Due to the relative motion between the GPS and the LEO satellite, a vertical scanning of the atmosphere is possible.

The advantages of the RO technique are numerous. Due to the low sensitivity of the emitted L-band microwave signals to aerosol, cloud and precipitation, the RO method is weather independent. The L-band signals not only enable measurements during day and night but can also penetrate clouds. This makes the RO method very useful for sensing weather phenomena with clouds and precipitation, like e.g., severe thunderstorms. Another characteristic of the RO technique is its high vertical resolution. It ranges from ∼0.1 km near the surface to ∼1 km at the height of the tropopause. The horizontal resolution, which lies between ∼100 and ∼300 km, is comparatively low. Since the RO method is insensitive to calibration

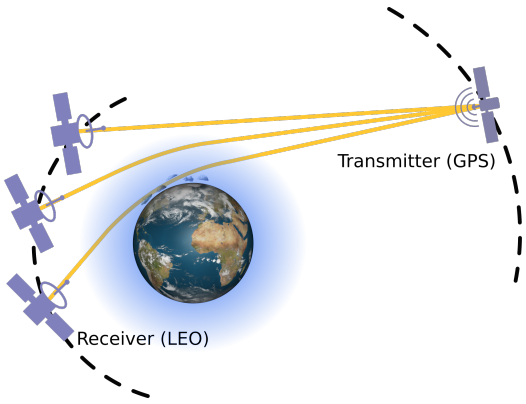

Figure 3.1.: RO principle (EODC 2019).

difficulties and instrument drift, it is also insensitive to instrument generation, a feature that allows to combine multiple measurements easily, which is very useful for long term climate monitoring. The number of RO events is linked to the number of available transmitters/receivers. A single receiver can collect about 250 RO profiles a day, that number can be doubled with an antenna for rising events. The 31 GPS satellites therefore ensure a high density of RO events distributed all over Earth (Jin et al. 2014; Foelsche et al. 2006).

3.1. Dry Atmosphere - Density, Pressure and Temperature

Since the atmosphere's density varies with height, a ray passing through it is refracted (Snell's Law) and delayed (Kursinski et al. 1997). After the phase delay gets processed to bending angles, it can be interpreted in terms of refraction via Abel transformation:

$$n(r_c) = \exp \frac{1}{\pi} \int_{a_1}^{\infty} \frac{\alpha}{\sqrt{a^2 - {a_1}^1}} da \,, \tag{3.1}$$

where α is the total bending angle, a the impact parameter, $a_1 = nr$ and r_c describes the distance from the centre of curvature. The obtained index of refraction can then be transformed into the atmospheric parameters mentioned before (Hajj et al. 2002; Kursinski et al. 1997). This transformation is possible because the atmospheric properties have an influence on the refractive index as expressed by the Smith-Weintraub-Equation (Smith and Weintraub 1953):

$$N = 77.6\frac{p}{T} + 3.73 \cdot 10^5 \frac{e}{T^2} - 4.03 \cdot 10^7 \frac{n_e}{f^2} + 1.4W \,, \tag{3.2}$$

where n describes the refractive index, p the atmospheric pressure in hPa, T the temperature in K, e the partial pressure of water vapor in hPa, n_e the electron density in m^{-3}, f the transmitter frequency in Hz and W the mass of condensed water in $\mathrm{g\,m}^{-3}$. Due to small vertical changes in the refractive index n, refractivity N is calculated via:

$$N = (n - 1) \cdot 10^6 \,. \tag{3.3}$$

The first term of equation 3.2 describes the contribution of the dry atmosphere, while the second term handles the contribution of the wet atmosphere. Even though the wet term is generally smaller than the dry one, it has a significant effect in the middle and lower troposphere, where it can make up to 30% of refractivity near the surface in lower latitudes (Jin et al. 2014). The influence of the ionosphere, which is described by the third term of the Smith-Weintraub-Equation, gets corrected up to the first order and leads to residual ionospheric errors. These errors systematically affect the accuracy of atmospheric parameters (Danzer et al. 2013). The fourth term, which describes the influence due to scattering on liquid water, can be neglected (Rieckh 2018). For dry regions (volume mixing ratio smaller than 10^{-4})

the moist term can also be neglected. This makes calculating the density fairly easy. The Smith-Weintraub-Equation is now reduced to $N = 77.6\frac{P}{T}$ and can be combined with the ideal gas law. This leads to density given as a function of refractivity:

$$\rho = \frac{p\bar{M}}{RT}\,, \tag{3.4}$$

where $\bar{M}$ is the mean molecular mass of dry air and $R = 8.314(\mathrm{J\,K^{-1}\,mol^{-1}})$ the universal gas constant. Pressure and temperature can be obtained by integration over the equation of hydrostatic equilibrium and by using the ideal gas law. (equations 3.5 & 3.6)

$$\frac{\partial p(r)}{\partial r} = -\rho(r)g\,, \tag{3.5}$$

$$p(r) = p(r_{top}) + \int_r^{r_{top}} \rho(r)g(r)dr = \frac{1}{77.6}N(r_{top})T(r_{top}) + \frac{\bar{M}}{77.6R}\int_r^{r_{top}} N(r)g(r)dr\,. \tag{3.6}$$

In order to obtain the pressure profile, an upper boundary condition of pressure $p(r_{top})$ is necessary, e.g. zero pressure at the top of the atmosphere ($p = 0$ when $r \to \infty$). One can also use the temperature from weather model analysis at high altitude. Temperature can be retrieved with equation 3.4 via:

$$T(r) = 77.6\frac{p(r)}{N(r)}\,. \tag{3.7}$$

This temperature is called dry temperature, in the case when water vapor is not negligible in lower altitudes. The dry temperature is colder than the real temperature (Jin et al. 2014).

3.2. Moist Atmosphere - Density and Water Vapor

In the middle and lower troposphere water vapor plays an important role and can therefore not be neglected. To derive water vapor, temperature and pressure from refractivity measurements one needs ancillary information for one of these three parameters (Kursinski et al. 1997; Jin et al. 2014). The Smith-Weintraub-Equation in combination with the ideal gas law can be expressed as:

$$\rho(r) = \frac{m_v}{77.6R}(N(r) - \frac{3.73\cdot 10^5 e(r)}{T^2(r)})\,, \tag{3.8}$$

where m_v is the mean molecular mass of moist air. Rearranging equation 3.2 leads to:

$$e(r) = \frac{N(r)T^2(r) - 77.6p(r)T(r)}{3.73\cdot 10^5}\,. \tag{3.9}$$

The retrieval of water vapor profiles is usually performed by applying either one of two common techniques.

3.2.1. Simple Retrieval

The simple retrieval method is commonly used due to its simplicity and its ease of calculation. Additionally, the simple retrieval is independent of first guess humidity. In the case of simple retrieval, T information from another source other than RO is used to calculate e via equation 3.9. Unfortunately, any possible error in T leads also to an error in e, which can result in an unphysical negative value for e (Rieckh et al. 2017). Since water vapor varies strongly and errors in T propagate into e, water vapor has usually a higher uncertainty than temperature and pressure (Jin et al. 2014). The errors in e due to errors in T can be estimated via the first order derivative of equation 3.2:

$$\delta e = \frac{1}{3.73 \cdot 10^5}(2NT - 77.6p)\delta T\,. \tag{3.10}$$

In addition to the errors of a-priori T, which dominate in the upper troposphere, RO errors also include errors of RO refractivity. These errors are caused by local multipath, receiver tracking errors and ducting (Rieckh 2018). Local multipath emerges due to multiple signals arriving at the GPS receiver antennas after they scattered off structures near the antenna. This leads to phase errors in the measurements. These errors can be reduced with more directional antennas or better modeling of the multipath near the receiver. Receiver tracking errors are the result of rapid fluctuations in phase and amplitude as well as a decreased signal-to-noise ratio (SNR). This mostly occurs in the moist lower troposphere, where the SNR decreases due to the atmospheric attenuation effect. As a solution to this problem another tracking technique was developed. The open loop technique is used in the moist troposphere, where sharp refractivity gradient and multipath have a big influence. Ducting occurs when the radius of the curvature of the ray is smaller than the radius curvature of the atmosphere r.

$$-\frac{dN}{dz} > \frac{10^6}{r} \approx 157[N - unit/km]\,. \tag{3.11}$$

The threshold in equation 3.11 is the so-called critical refraction. This effect results in negative errors in the RO refractivity below the ducting layer (Jin et al. 2014).

3.2.2. 1D-Var Retrieval

Another way of retrieving water vapor profiles from measurements of N is the so called 1D-Var method. In this procedures, instead of using T information from ancillary sources, adjusted a-priori profiles of T and e are used (Rieckh et al. 2017). This adjustment is executed in a way that is consistent with the estimated background errors which finds the optimal solution to the state vector x. This solution can be achieved by minimizing a cost function $J(x)$:

$$J(x) = \frac{1}{2}(x - x^b)^T B^{-1}(x - x^b) + \frac{1}{2}(y^o - y(x))^T (O + F)^{-1}(y^o - y(x)) \,, \quad (3.12)$$

with the state vector x (e.g. e), the measurement vector y (e.g. N from RO) and the forward model $y(x)$ which maps the state vectors in the measurement space. b and o stand for the background/measurement information. O and F are the error covariance of the measurement and the forward model. Under the assumption of unbiased, uncorrelated errors and a Gaussian distribution. The minimum of the cost function can be found iteratively but there is always a risk that the algorithm stops at a local minimum of J (Rieckh 2018).

In the case of 1D-Var retrieval, results are less sensitive to the errors in the a-priori information than in the simple retrieval. Nevertheless, errors of the 1D-Var retrieval are harder to interpret since they consist of the errors of the model background errors (Jin et al. 2014). The 1D-Var retrieval leads to better results in the mid and upper troposphere but has the disadvantage that it is a far more complex method than the simple retrieval (Rieckh 2018).

Part II.

Datasets, Events, and Methods

4. Data

4.1. Radio Occultation Data

A single radio occultation measurement has a horizontal scale of about 300 km, hence the daily horizontal resolution is comparatively low (Fu et al. 2007). To solve this problem RO data usually are averaged over time, longitude, and latitude. In this work the radio occultation data from Brunner et al. (2016) were used. These data were processed with the Wegener Center occultation processing system version 5.6 (OPSv5.6). Observations from multiple RO missions were included such as the CHAllenging Minisatellite Payload (CHAMP) (GFZ 2019), the Gravity Recovery and Climate Experiment (GRACE) (GFZ 2008), and the Constellation Observing System for Meteorology, Ionosphere and Climate (COSMIC) (Atmospheric Research 2019a). From the RO profiles the following variables were derived: density, pressure, geopotential height (GPH), potential temperature, and tropospheric water vapor. A weighted average was applied to the RO profiles to obtain daily fields on a 2.5° x 2.5° grid:

$$x_{grid}(\lambda, \phi, d) = \frac{\sum_i w_i x_i(\lambda', \phi', d')}{\sum_i w_i}\,, \tag{4.1}$$

where $x_{grid}(\lambda, \phi, d)$ is an atmospheric variable (f.e. temperature) at a specific point at longitude λ, latitude ϕ and day d. $x_i(\lambda', \phi', d')$ is an individual atmospheric profile at the RO event location (λ', ϕ') and day d'.
To minimize the number of bins with no measurements, without losing too much resolution of atmospheric variability, all RO events within ± 7.5° in longitude, ± 2.5° in latitude, and ± 2 days were included and weighted by a Gaussian weighting function. For longitude and time the weighting function w_i is given by equation 4.2.

$$w_i = \exp\left(-\left[\left(\frac{\Delta\lambda}{L}\right)^2 + \left(\frac{\Delta d}{D}\right)^2\right]\right)\,, \tag{4.2}$$

where $L = 7.5°$ and $D = 1$ day. Due to this weighting about 80% of the grid cells (for an exemplary day) contain information of at least four RO profiles. The number of profiles decreases only near the equator and close to the poles, which leads to very few bins without any information at all (Brunner et al. 2016).

4.2. ECMWF reanalysis and forecasts

As a comparison to the RO data, reanalysis and forecasts from the European centre for Medium-Range Weather Forecasts (ECMWF) were used.

4.2.1. Integrated Forecasting System

The Integrated Forecasting System (IFS) is an atmospheric model and data assimilation system developed at the ECMWF in cooperation with Météo-France, which forms the basis for all data assimilation and forecasting activities of the ECMWF. To model atmospheric dynamics correctly, the IFS has a dynamical core which discretises the Euler equations of motion. The core of the IFS is not only hydrostatic but also semi-Lagrangian, two-time-level and semi-implicit. Making the core semi-Lagrangian allowed bigger time steps to be used before reaching numerical instability (before only time steps of max. 3 min were possible). Horizontally a reduced Gaussian grid is used, which means that the grid points along a circle of latitude decrease towards the poles whereby computation time is reduced significantly. Vertically the IFS uses a finite-element scheme to discretice the model. The schemes implementation in the IFS lead to errors that are 8 times smaller than those of similar schemes (ECMWF 2019c; Woods 2005).
In this work the data used were processed at the Wegener Center for Climate and Global Change. They are given on a full Gaussian grid with 32 latitude lines between the pole and the equator with a spectral resolution of 64x128 (lat x lon) which corresponds to a spacing of 310 km (2.79°) at the equator. In the vertical a log-linear spline interpolation was used and in the horizontal a polynomial interpolation. As a reference geoid the EGM2008 with the WGS84 as a reference ellipsoid was applied.

4.2.2. Reanalysis

The ECMWF uses its forecast models and data assimilation systems to reanalyze observations of the past. The reanalyses give a numerical description of the recent climate with respect to the atmosphere, land surface, and the oceans. Since these reanalyses are used for, e.g., climate change monitoring, it is desirable to have consistent reanalyses of the coupled climate system, which is, at the moment, also the focus of reanalysis research at the ECMWF (ECMWF 2019a). The reanalyses used in this thesis are based on the previously described IFS.

4.2.3. Forecasts

A forecast is based on the current state of the atmosphere. In order to estimate this initial condition, the ECMWF uses data assimilation from, e.g., satellites, weather stations, ships, and buoyes. The process of data assimilation is a sequential time-stepping procedure, which means that a previous forecast is compared to new observations and updated accordingly. Since the atmosphere is chaotic, a small

difference in its state can have many different weather patterns as an outcome. To account for this problem, the ECMWF runs 51 forecasts simultaneously, where one forecast uses the best initial state and the others slight variations. Therefore not only possible weather patterns can be predicted, but also how likely they will occur (ECMWF 2019b).

5. Selected Precipitation Events

The aim of this work is to assess whether Mediterranean low pressure systems, which caused heavy precipitation events in Austria, can be detected in radio occultation data. For this purpose well known precipitation events in the years 2009, 2010, 2013, and 2014 were chosen and analyzed. A short description of these events is given in this chapter.

5.1. June 22nd to June 25th 2009

From June 22nd to June 25th 2009 over 100 mm rain fell in Upper and Lower Austria as did in parts of Salzburg. The southeastern part of Lower Austria lay in the centre of this event, where more than 200 mm were measured. In Styria and Burgenland this amount of rainfall was close to the amounts of a 50 year event. The reason for this event was an upper low-pressure system that came from middle Italy. It stayed multiple days nearly stationary above the Adria, where it absorbed warm moist air before it moved over the Balkans towards eastern Europe. Later the system hit against the Alps from northeast where orographic lifting intensified the heavy rainfalls even more. In contrast to the rainfalls at the north of the Alps, the precipitation in Styria and Burgenland was intensified due to convective cells that formed. Figure 5.1 shows the amount of precipitation above Austria during this event (Haiden 2009).

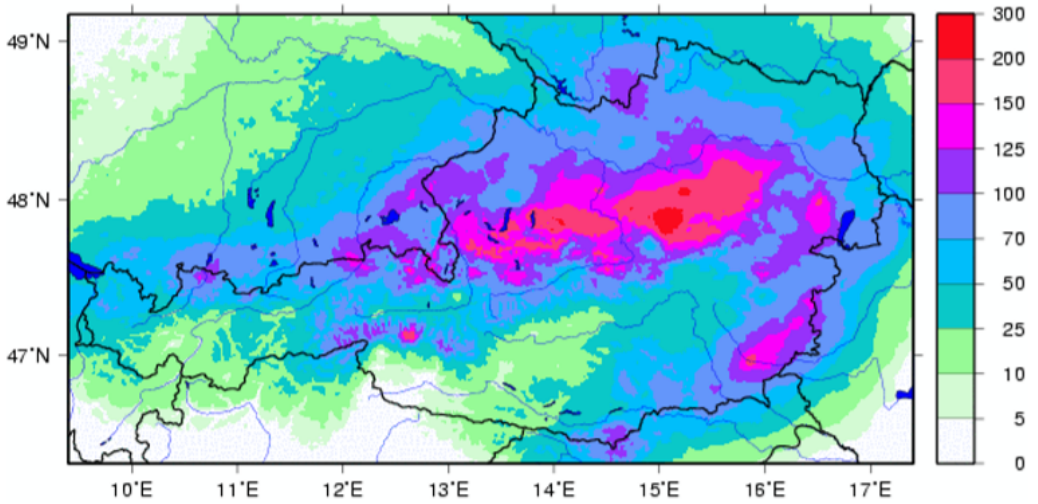

Figure 5.1.: Amount of precipitation between June 22nd and June 25th 2009 given in mm (Haiden 2009).

5.2. March 7th to March 12th 2010

An Adriatic low (Andrea) in combination with a North Middle European high (Isidor) caused severe snowfalls in the Mediterranean, starting at the 8th of March 2010. Even though there was no heavy precipitation due to this event in Austria, it is nevertheless an interesting event. Heavy snowfalls in Italy, Croatia, and Spain caused chaos and severe damage. In Croatia a snow cover with a thickness up to 70 cm was reported while on Mallorca the use of non-skid chains was necessary. In Italy it snowed uninterrupted for 24h which lead to the closure of the Marconi airport near Bologna and to the stranding of a transport ship (Zeit 2010). Figure 5.2 shows the weather maps of this event.

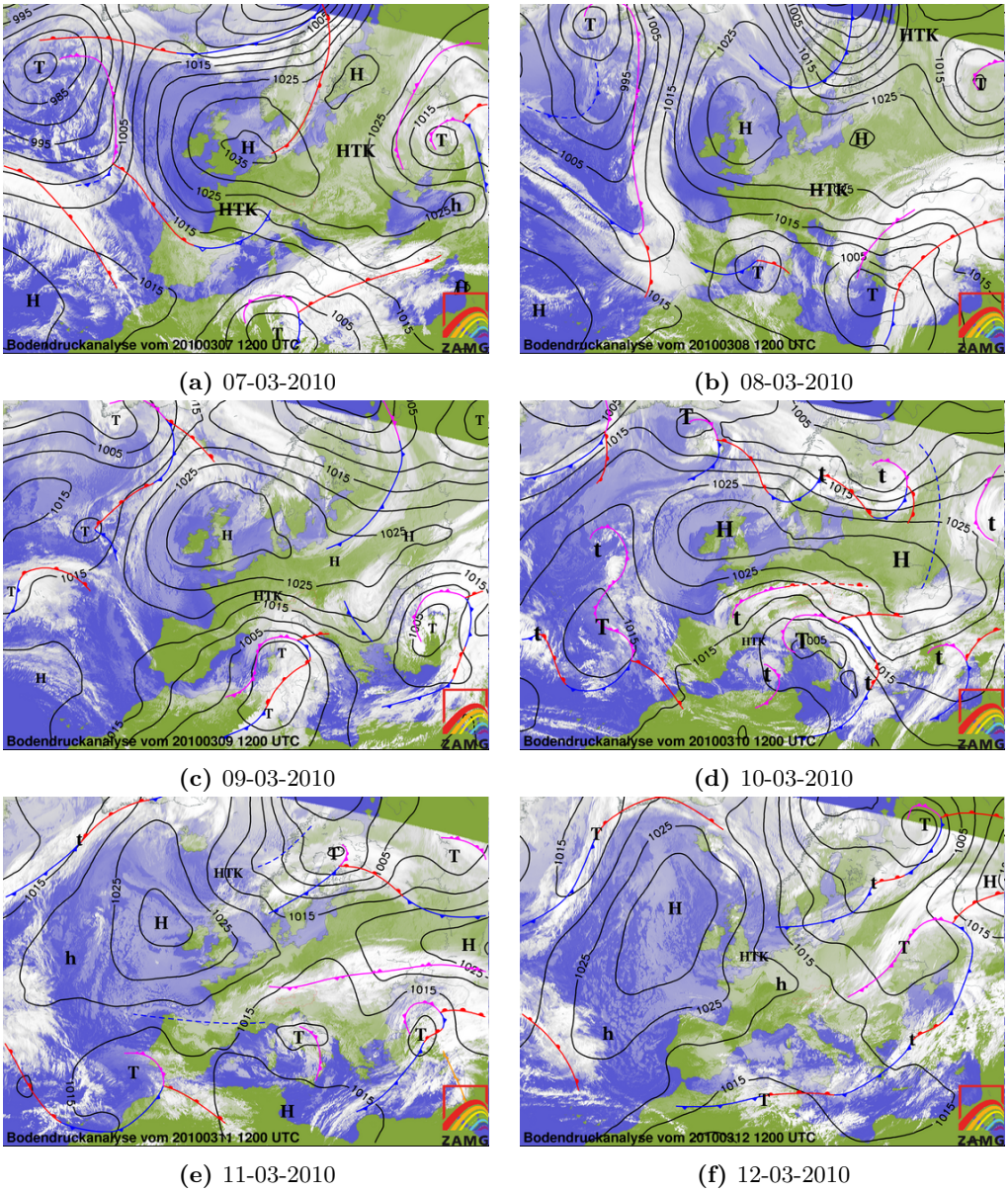

(a) 07-03-2010 **(b)** 08-03-2010

(c) 09-03-2010 **(d)** 10-03-2010

(e) 11-03-2010 **(f)** 12-03-2010

Figure 5.2.: Weather Maps Event March 2010.
Red lines with semicircles mark warm fronts, blue lines with triangles mark cold fronts, pink lines describe occulsions and dashed blue lines trough lines. HTK ("Höhentiefkern") denotes Upper Level Lows, while H,h,T, and t, denote the centres of the Highs (German "Hoch") and Lows (German "Tief"), lower case letters mark local maxima/minima (ZAMG 2019a).

5.3. May 2010

The amount of sunshine during May 2010 is amongst the three lowest since the beginning of measurements in 1880. While March and April 2010 were unusually dry, the precipitation amounts in May were up to three times larger than the long time average. In Poysdorf (Lower Austria) 350% of the average precipitation was measured, which makes it the wettest May in the 44 year long time series. Responsible for these high amounts of precipitation in Eastern and Northern Austria was a stable Adriatic low pressure system, which brought heavy rainfalls in the middle of May. In addition to the Adriatic low-pressure system, many thunderstorms occurred and intensified the heavy rainfalls (ZAMG 2010).

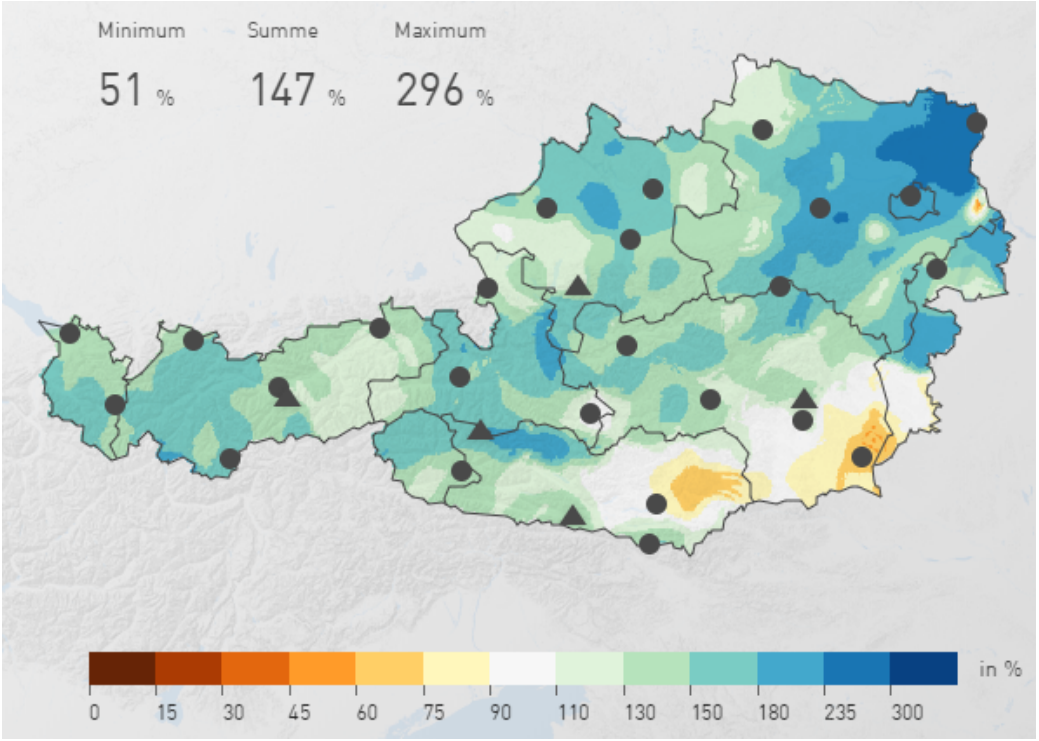

Figure 5.3.: Comparison of the precipitation amount to the mean of 1981-2010, 100% correlate with the mean. Circles mark weather stations, triangles mark weather stations on mountains. "Summe" gives the total amount of anomalies (ZAMG 2019b).

5.4. May/June 2013

Since the beginning of precipitation measurements in Austria, May 2013 was one of the three wettest Mays (besides May 1962 and May 1965). While there was 20% less sunshine in comparison to the mean of 1981-2010, the amount of precipitation was 200% of the usual amount. Especially towards the end of May 2013, heavy

rainfalls in Vorarlberg, Tyrol, and Salzburg, caused floods and mud flows. In June the rainfalls shifted to the northern half of Austria, where up to 150% of the usual amount of precipitation fell. In contrast to these rainfalls, the southern part of Austria was very dry, with only 21 mm precipitation in Villach (Carinthia) (ZAMG 2013a; ZAMG 2013b). Figure 5.4 shows the precipitation amount for May and June 2013 in comparison to the mean of 1981-2010.

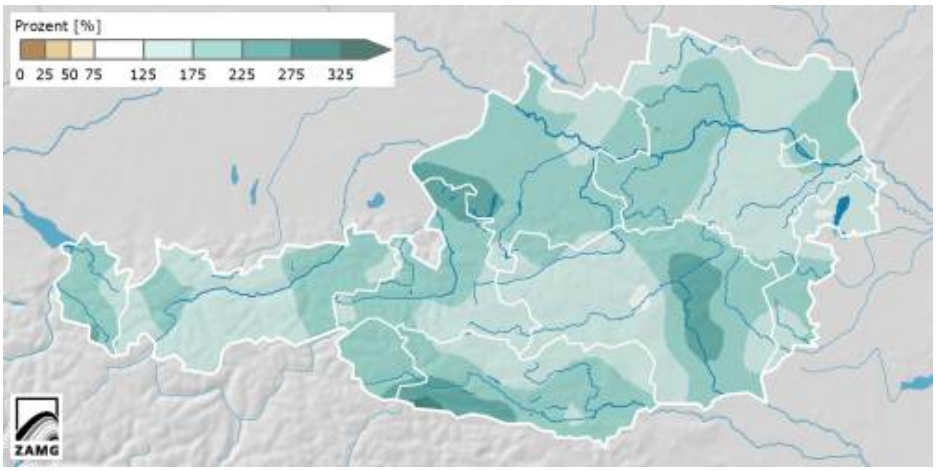

(a) May 2013

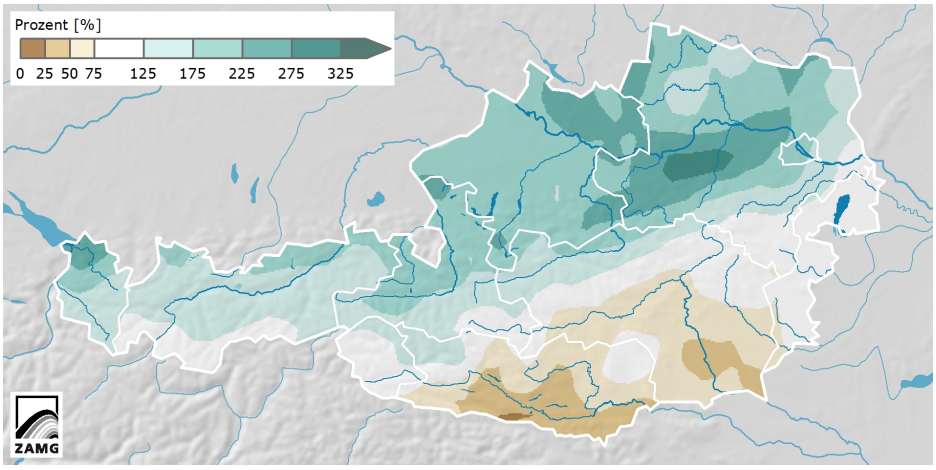

(b) June 2013

Figure 5.4.: Comparison of the precipitation amount to the mean of 1981-2010, 100% correlate with the mean (ZAMG 2013a; ZAMG 2013b).

5.5. November 2014

November 2014 was the warmest November since Austrian measurements started in 1767. With temperatures that lay 3.8 °C above the mean from 1981-2010, it was

the 9th month of 2014 that was unusually warm. While it was a very dry month north of the Alps, 25-242% more precipitation than usual fell in the area of eastern Tyrol, Carinthia and Southern Styria. Within the first six days of November, the amount of rain that fell in eastern Tyrol and Carintha exceeded the usual amount of rain for the whole month (ZAMG 2014b). This heavy rainfalls were a result of multiple low pressure systems above Europe (ZAMG 2019a):

- **Pia** already formed at the end of October above the North Atlantic and moved over the UK towards the North Sea, where it dissolved around the 5th of November.
- **Qendresa** was a low pressure system that formed above Italy around the 4th of November. It moved westward over the Ligurian Sea and triggered heavy rainfalls above Middle and Northern Italy.
- **Roswita** formed near Iceland and weakened the foehn on the 6th of November.
- **No name** was an unnamed low-pressure system that formed above Italy.
- **Stephanie** formed around the 9th of November above the Atlantic and later moved towards Europe.

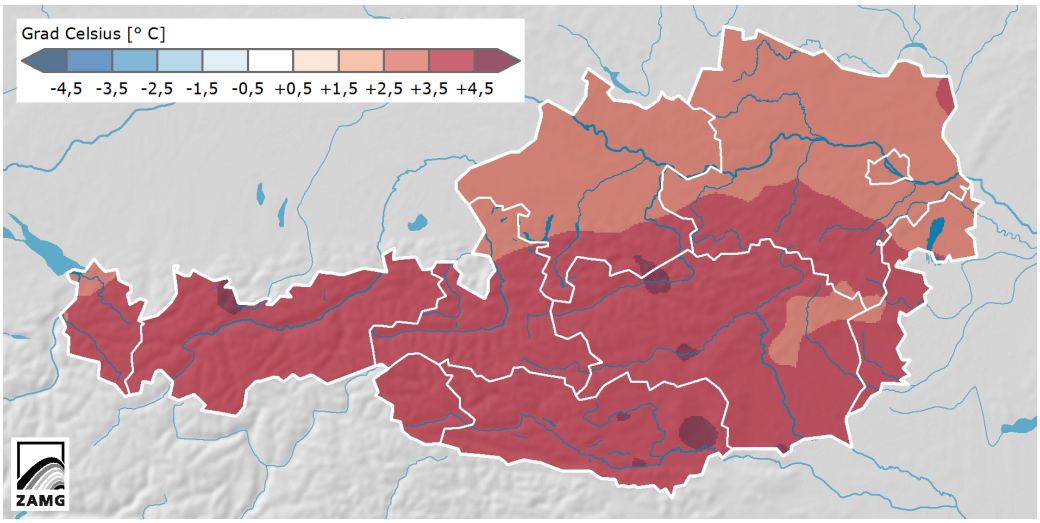

(a) Temperature Anomalies from the mean of 1981-2010.

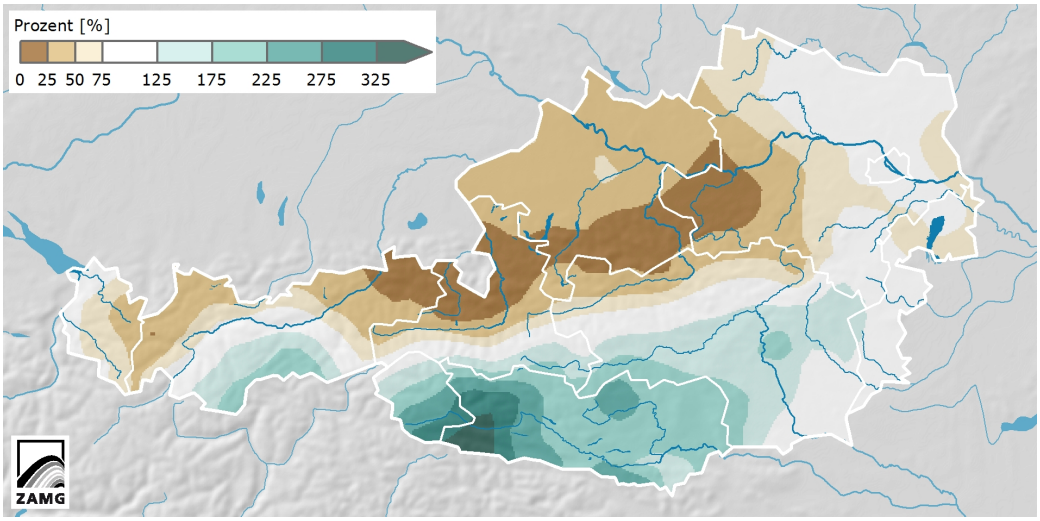

(b) Comparison of the precipitation amount to the mean of 1981-2010, 100% correlate with the mean.

Figure 5.5.: Temperature and precipitation anomalies November 2014 (ZAMG 2014b).

6. Methods

6.1. Integrated Water Vapor

As mentioned in subsection 1.4, the Integrated Water Vapor (IWV) is calculated via $IWV = \int_0^\infty \rho_w dz$ (Equation 1.14). Using the relation between absolute humidity ρ_w, specific humidity q, and density ρ:

$$q = \frac{\rho_w}{\rho}\,, \tag{6.1}$$

equation 1.14 can be written as:

$$IWV = \int_0^\infty \rho q dz\,. \tag{6.2}$$

The ECMWF data include the parameters temperature, pressure, specific humidity, and geopotential height in dependence of height. Equation 6.2 can therefore be applied to these data without further rearranging of equation 1.14.
The parameters in the RO data are given in dependence of pressure instead of height. To calculate the IWV a variable transformation, using the barometric height formula (Eq. 1.1), is necessary:

$$\frac{dp}{dz} = -\rho \cdot g\,, \tag{6.3}$$

$$dz = -\frac{dp}{\rho g}\,, \tag{6.4}$$

with g being the gravitational acceleration, which is assumed to be constant: $g = 9.81\ \mathrm{m\,s^{-2}}$. Inserting equations 6.1 and 6.4 into equation 1.14 leads to:

$$IWV = -\int_{p_0}^{0} q\frac{dp}{g}\,. \tag{6.5}$$

6.2. Averaging of the ECMWF data

As described in section 4.1, all RO events within ± 7.5° in longitude, ± 2.5° in latitude, and ± 2 days were included and weighted by a Gaussian weighting function to reduce the number of bins with no measurements. Since reanalyses and forecasts from the ECMWF are used as a comparison, these data have to be averaged as well. For every data point all points within ± 2.5° in latitude and ± 2 days were averaged with a Gaussian window. Using a Gaussian window for

the averaging in longitude lead to *nan* values at lower altitudes. Since the lower altitudes are the most important in this work, a Blackman window was used for the averaging instead, and all points within ± 7.5° in longitude were included.

6.3. Precipitable Water RO and ECMWF

To assess whether Mediterranean low-pressure systems can be detected in specific humidity data from RO measurements, the PW is plotted. The relation between PW and IWV can be obtained by inserting the unit of the IWV ($\mathrm{kg\,m^{-2}}$) and $\rho = 1000\mathrm{kg\,m^{-3}}$ into equation 1.13:

$$1\mathrm{kg\,m^{-2}}\, IWV = 1\mathrm{mm}\, PW\,. \tag{6.6}$$

For comparing reasons, the absolute and relative difference between PW_{RO} and PW_{ECMWF} were calculated via equations 6.7 & 6.8.

$$\Delta PW_{abs} = PW_{RO} - PW_{ECMWF}\,, \tag{6.7}$$

$$\Delta PW_{rel} = \frac{PW_{RO} - PW_{ECMWF}}{PW_{ECMWF}} \cdot 100\%\,, \tag{6.8}$$

where PW_{RO} denotes the PW value of the RO data, and PW_{ECMWF} the PW value of the ECMWF data.

6.4. Low-Pressure System Tracks

In order to see if the low-pressure systems seen in the PW plots match the described events, the paths of the lows were calculated. For each grid point the calculated PW values over time were plotted as a time series. As indicated in figure 6.1 the maxima of these time series are different for each grid point. This was used to create plots that show the date of the maxima in the PW value for each grid point. The later the maximum occurred, the darker the grid point is depicted. The path can therefore roughly be retraced.

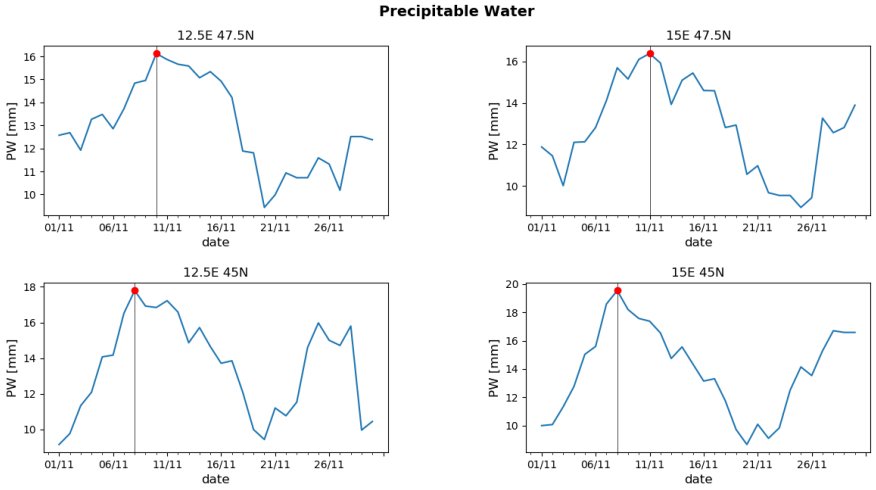

Figure 6.1.: *PW* time series for 4 grid points above Austria and their maxima

6.5. Specific Humidity Vertical Structure

A huge difference between the RO data and the ECMWF data is that the ECMWF data includes measurements down to the Earth's surface, while RO measurements start at higher altitudes. To asses whether this influences the ability of detecting high precipitation events beginning at a certain altitude, the vertical structure of the specific humidity measurements (RO and ECMWF) were plotted and compared. For RO this imposed no problem but since the ECMWF data sets are given in dependency of height instead of pressure an interpolation of the ECMWF data on the pressure grid of the RO data had to be applied first. The specific humidity is plotted for each day up until a pressure level of 500 hPa for four neighboring grid points (2x2). Since these profiles don't differ significantly from each other, they were averaged. To compare the results of the RO data to the ones of the ECMWF data, the absolute (Eq. 6.9) and relative difference was calculated (Eq. 6.10):

$$\Delta q_{abs} = q_{RO} - q_{ECMWF}\,, \tag{6.9}$$

$$\Delta q_{rel} = \frac{q_{RO} - q_{ECMWF}}{q_{ECMWF}} \cdot 100\%\,, \tag{6.10}$$

with q_{RO} being the specific humidity values of the RO data, and q_{ECMWF} being the specific humidity values of the interpolated ECMWF data. Δq_{abs} is in units of $\mathrm{g\,kg^{-1}}$,while Δq_{rel} is in %.

Part III.

Results, Discussion, and Conclusions

7. Low-Pressure Systems in PW data from RO Measurements

7.1. Event 2009

To investigate the precipitation event in 2009, data from June 18$^{\text{th}}$ to July 31$^{\text{st}}$ were analyzed. As described in section 5.1, the reason for the high precipitation amounts during this event was an upper low-pressure system that came from Middle Italy and moved over Eastern Europe before it hit Austria from the northeast. Figure 7.1 shows this path clearly.

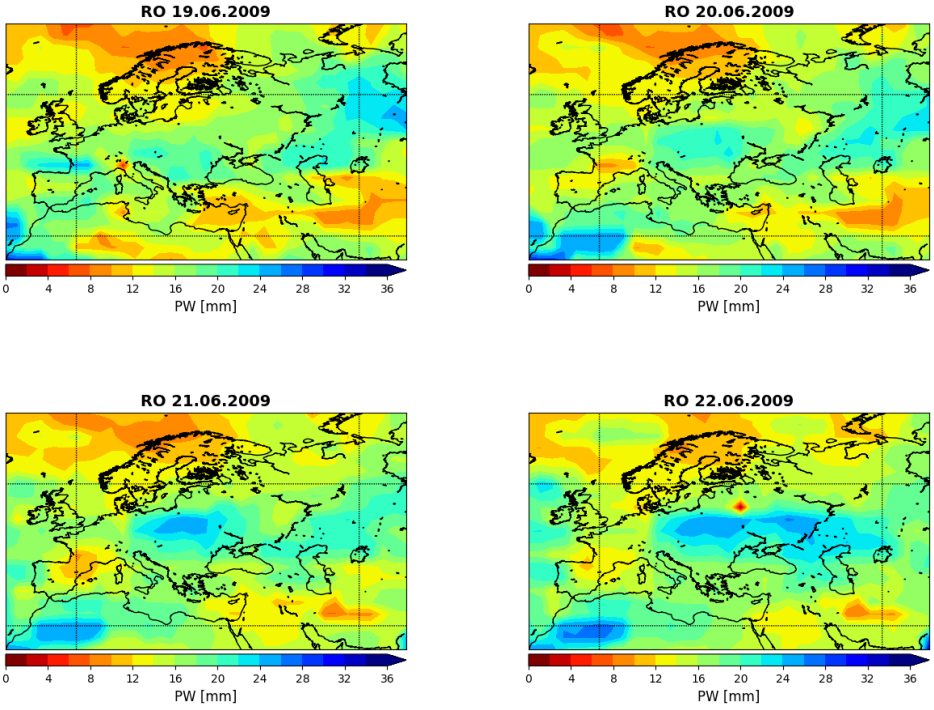

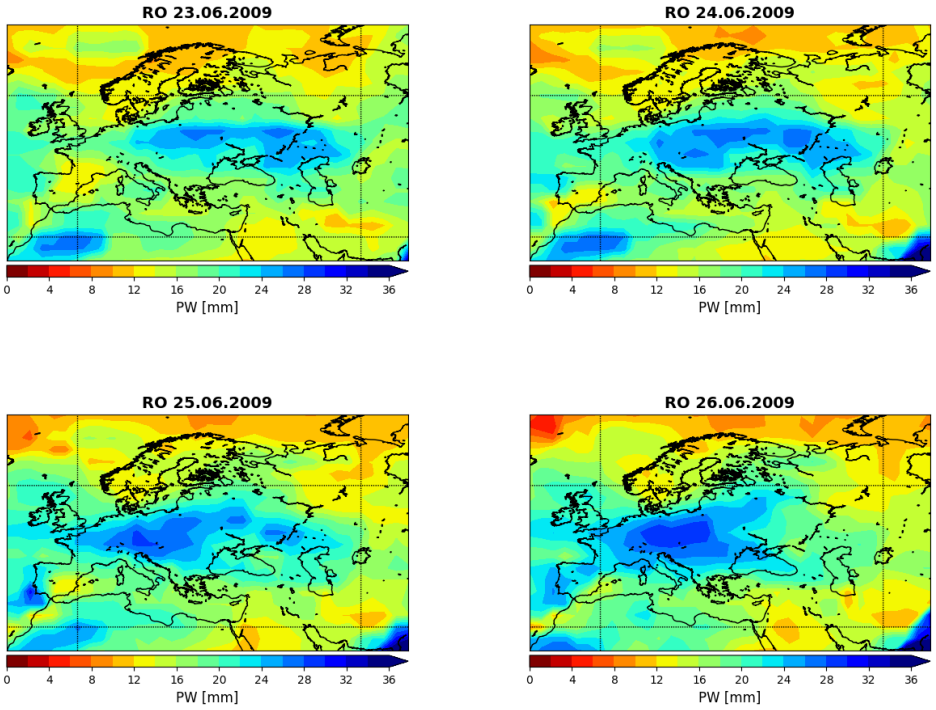

Figure 7.1.: *PW* event 2009

Before the low reached Austria, the *PW* value in this region was about 20 mm. During the event this amount increased and reached values of about 28 mm, before it decreased again to 18 mm at the beginning of July (around the 8^{th}). In addition to the previously described event, a few smaller lows can be seen in the plots, such as a Mediterranean low near Genoa. It formed around July the 7^{th} and moved northward where it dissolved on the 13^{th} of July (Figure 7.2).
Besides the described events, the *PW* plots also show that the period of June/July 2009 was very wet in general, which makes detecting local low-pressure systems more difficult.

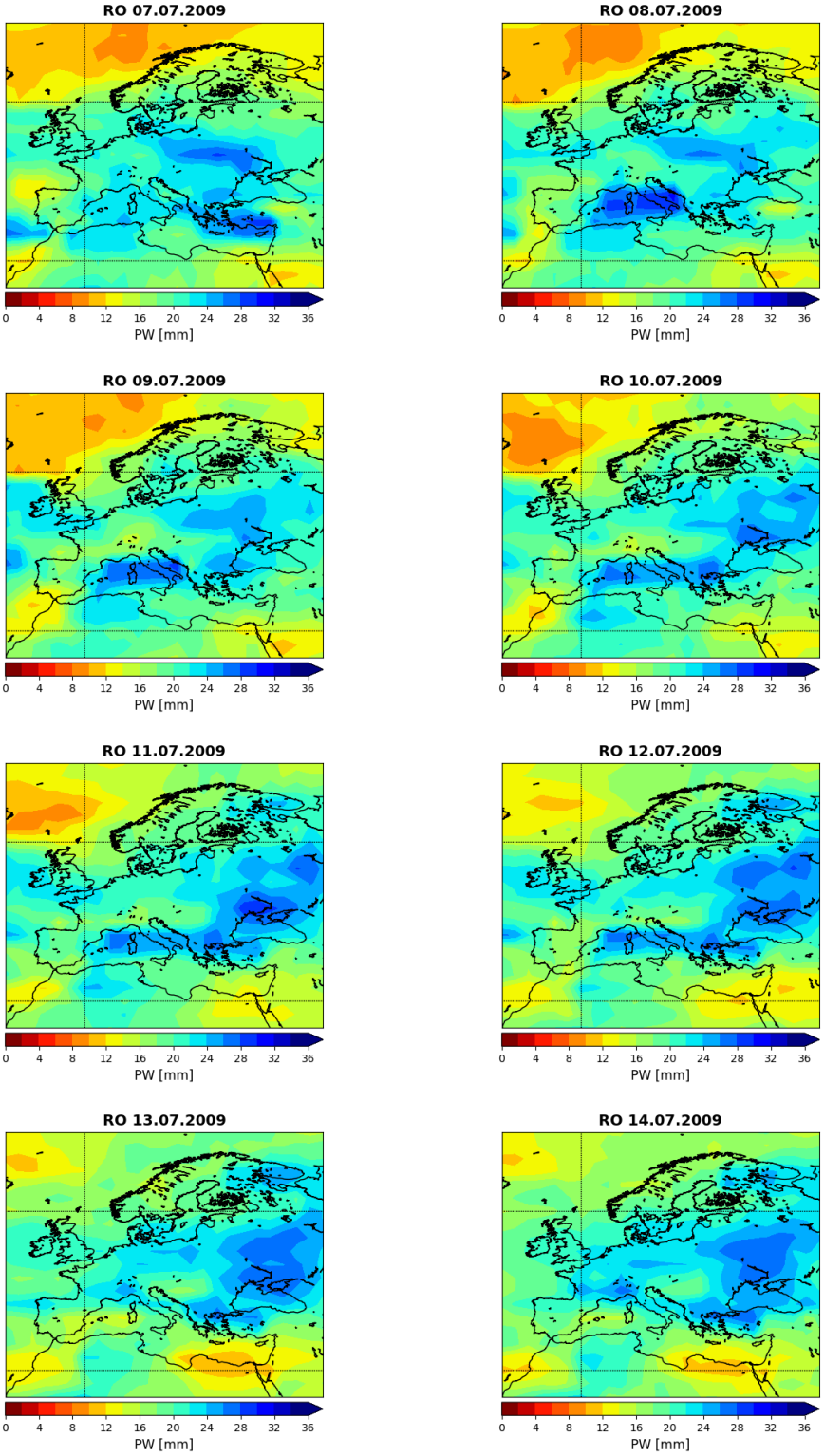

Figure 7.2.: *PW* Genoa Low 2009

7.2. Event 2010

The Adriatic low-pressure system which brought heavy rainfalls to Austria in the middle of May 2010, can hardly be seen, even within a smaller *PW* range (Figure 7.3).

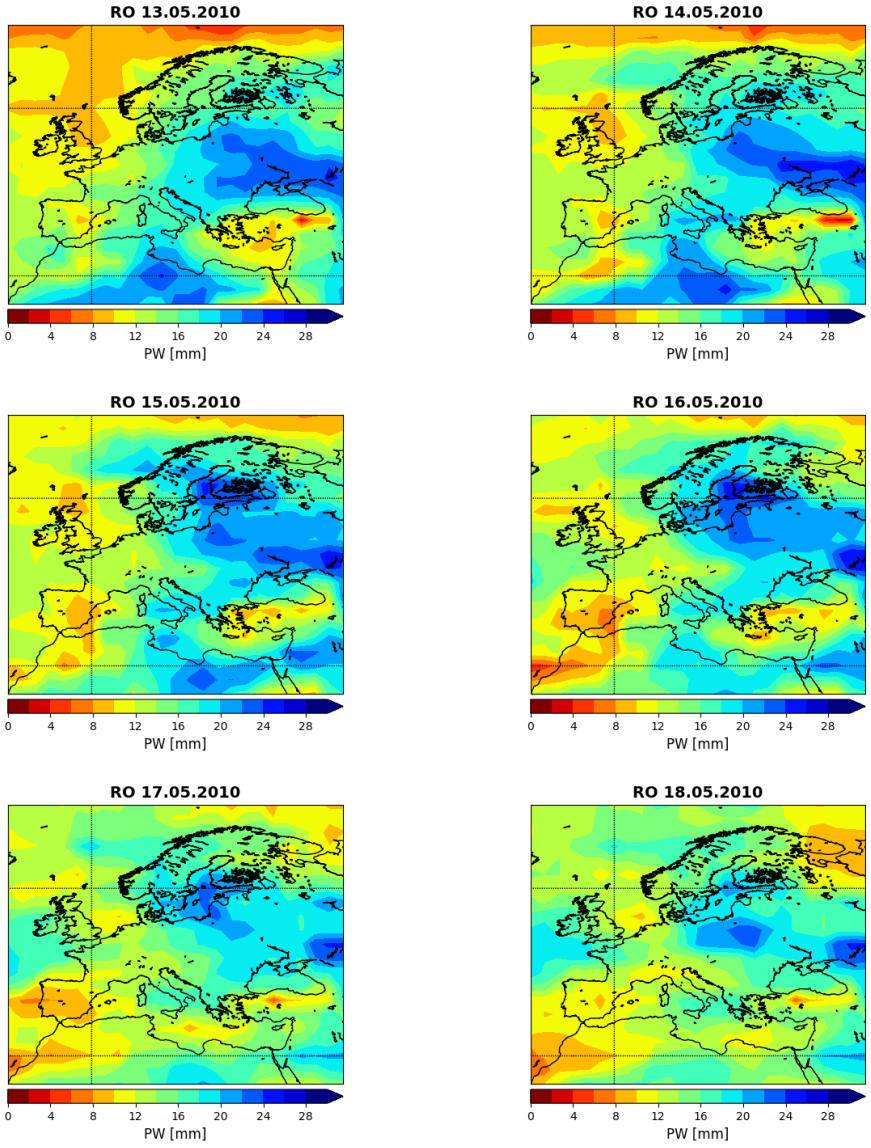

Figure 7.3.: *PW* Adriatic Low 2010

Starting at the 28th of May, the *PW* values were significantly higher than before. All over Europe, the high *PW* values persisted and didn't start to decrease even at the end of the investigated period on the 31st of July (Figure 7.4).

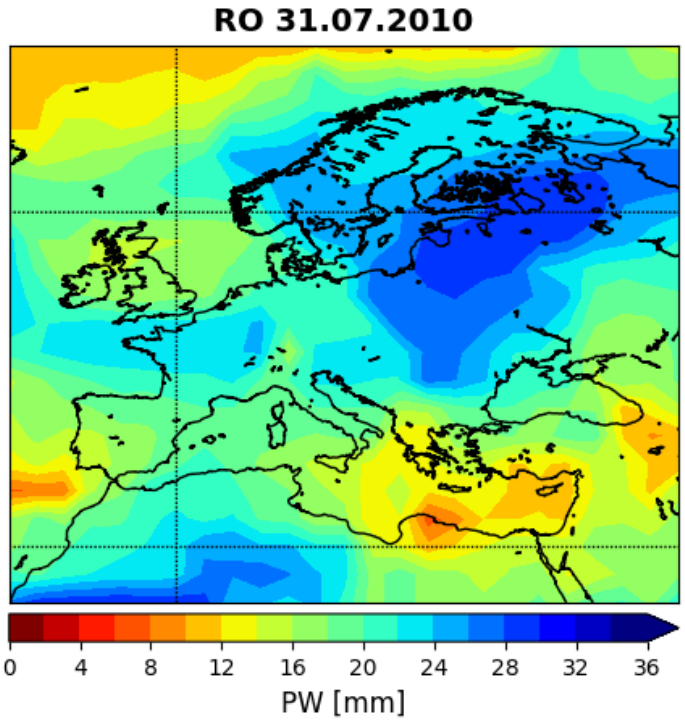

Figure 7.4.: *PW* on the 31st of July 2010.

7.3. Event 2013

The situation in 2013 was similar to the one in 2010. At the beginning of May increased values of *PW* above the Adriatic Sea and Austria can be seen (Figure 7.5). Nearly a month later, on the 2nd of June, the *PW* increased again and persisted until the end of July. At the end of the investigated period a decrease is not yet in sight.

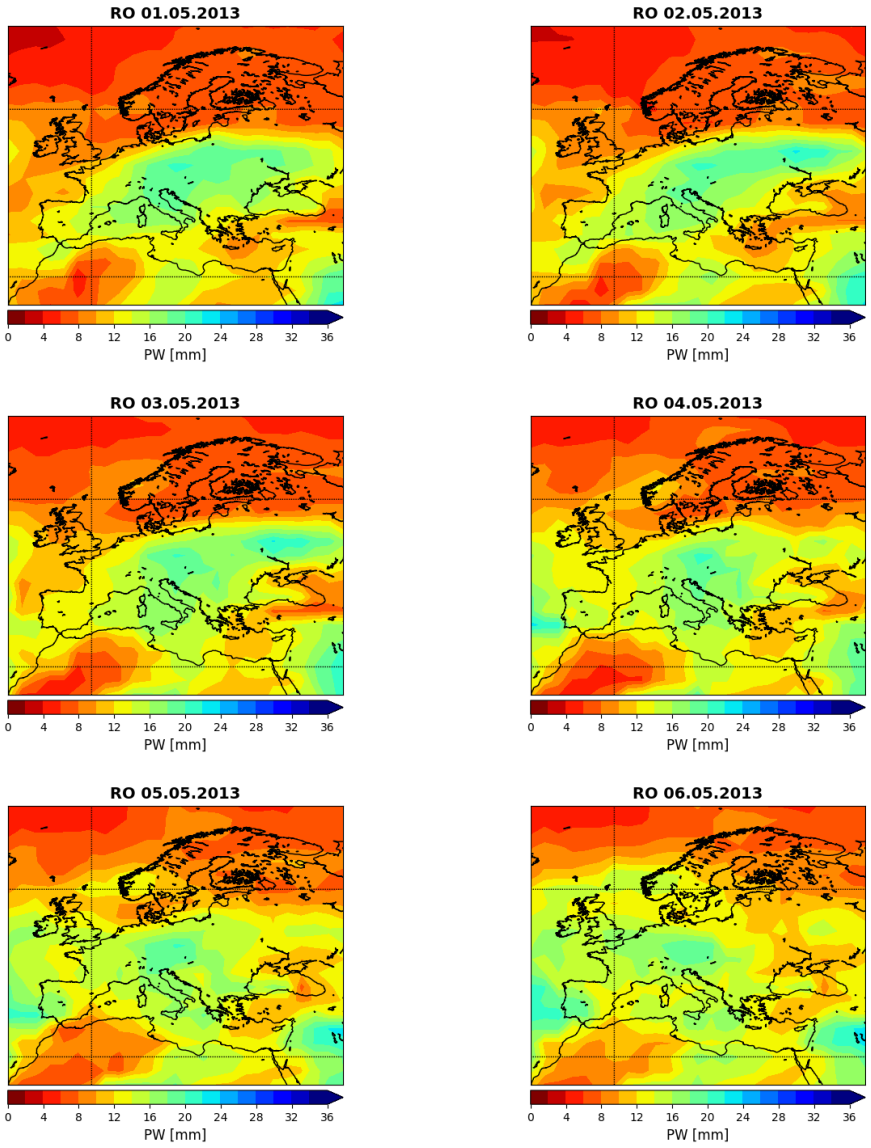

Figure 7.5.: *PW* Beginning of May 2013

7.4. Event 2014

As described in chapter 5.5, the amount of rain that fell within the first six days of November 2014, exceeded the usual amount of rain for the whole month. Figure 7.6 shows the *PW* values for these days.

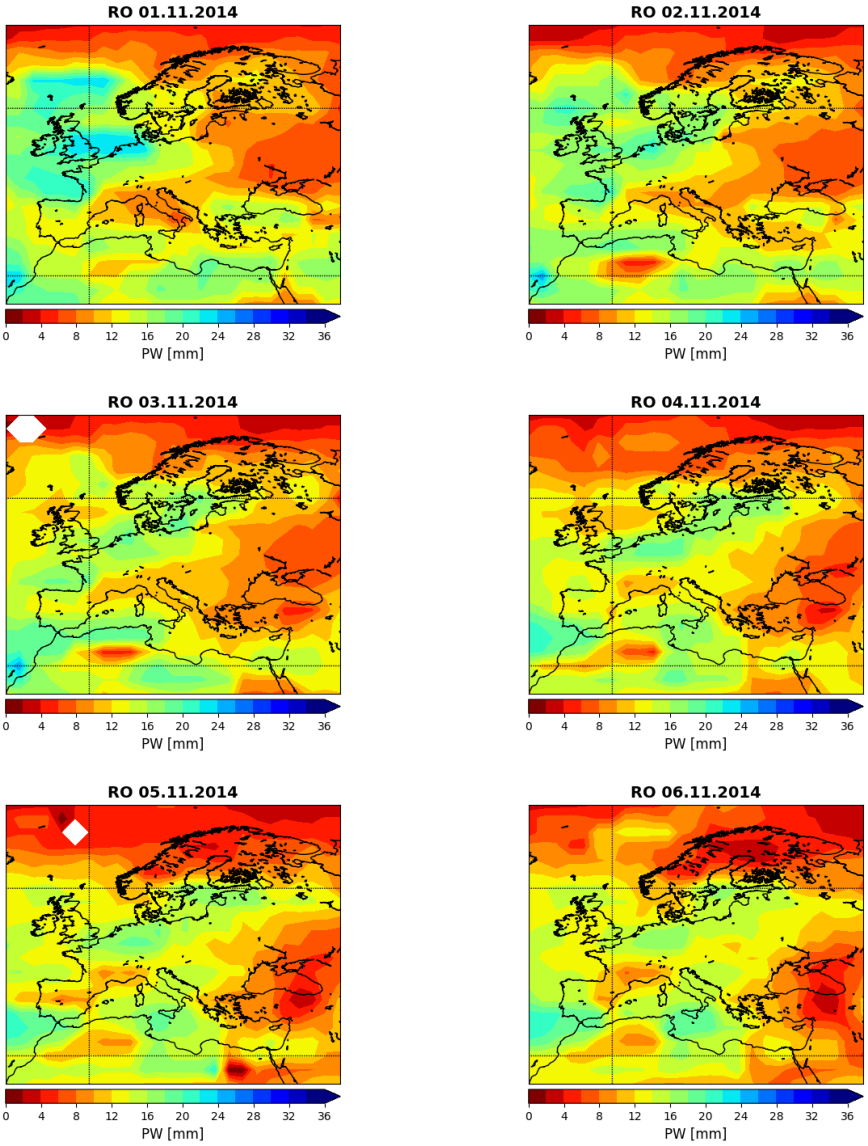

Figure 7.6.: *PW* Beginning of November 2014

Within these figures the high amount of precipitation above Austria can't be seen clearly. At the fourth of November an area of increased *PW* values starts to form

near Sicily. This low-pressure system later moves northward towards Austria, where it dissolves around the thirteenth of the month (Figure 7.7).

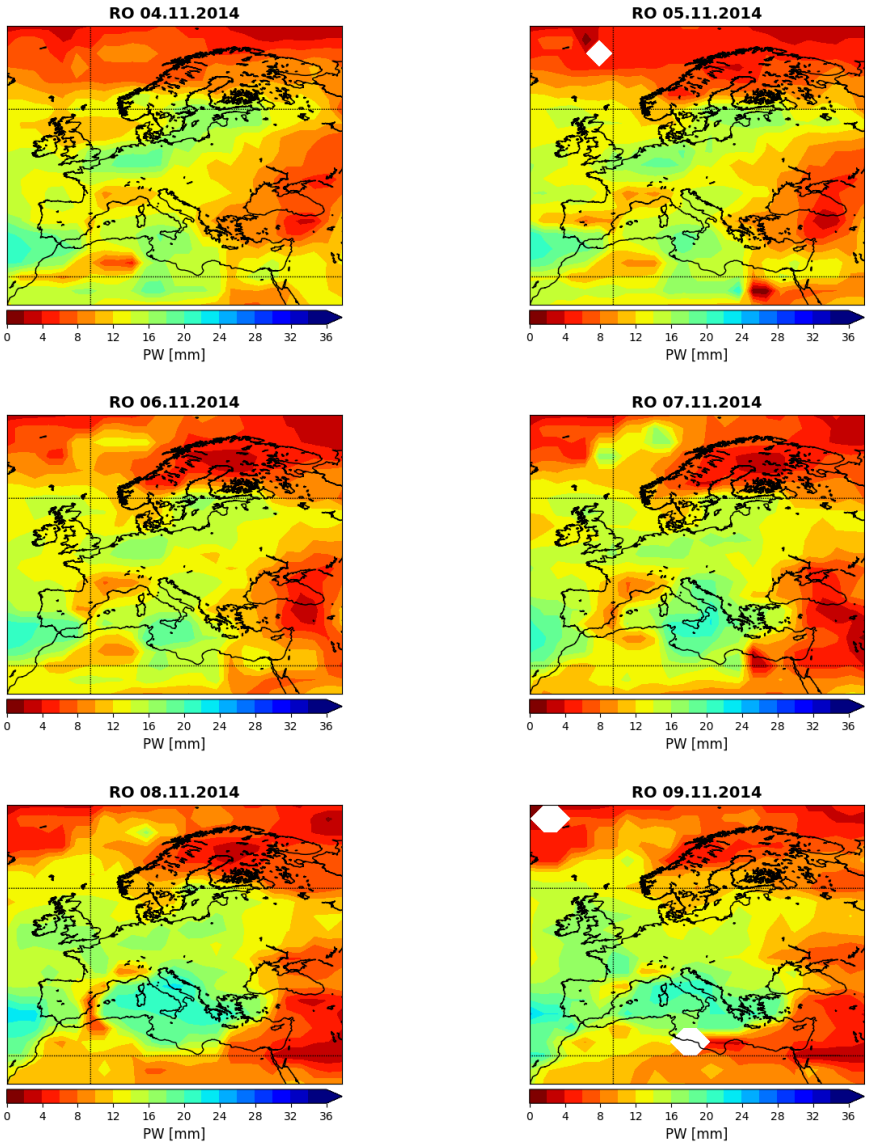

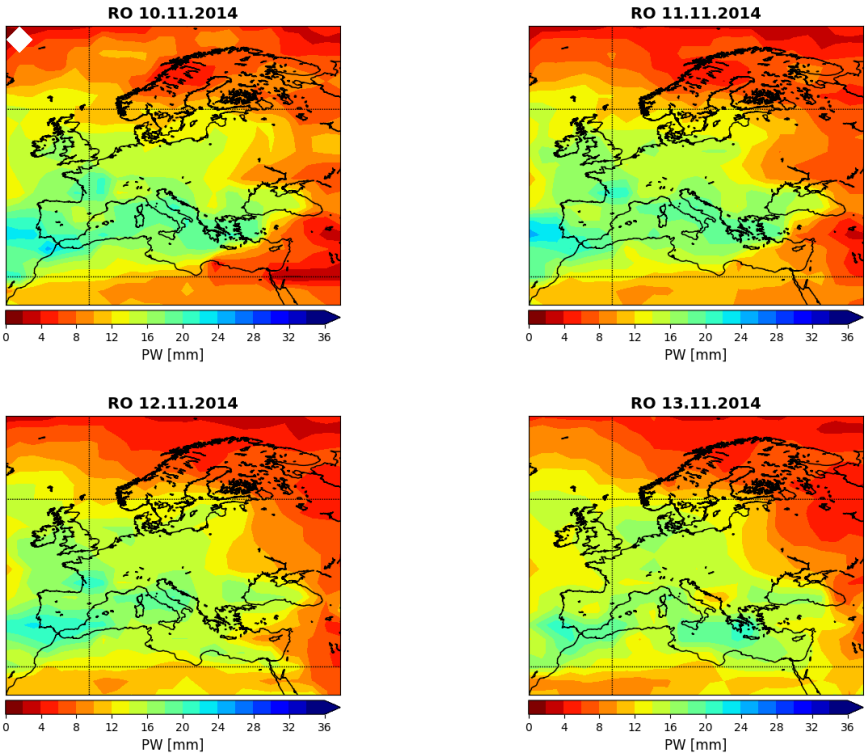

Figure 7.7.: *PW* 4$^{\text{th}}$ to 13$^{\text{th}}$ of November 2014

Another low-pressure system, which forms around the 21st in the Western Mediterranean, can be seen in the *PW* plots (Figure 7.8). This system continues to move northward until the end of the investigated period on the 30th of November.

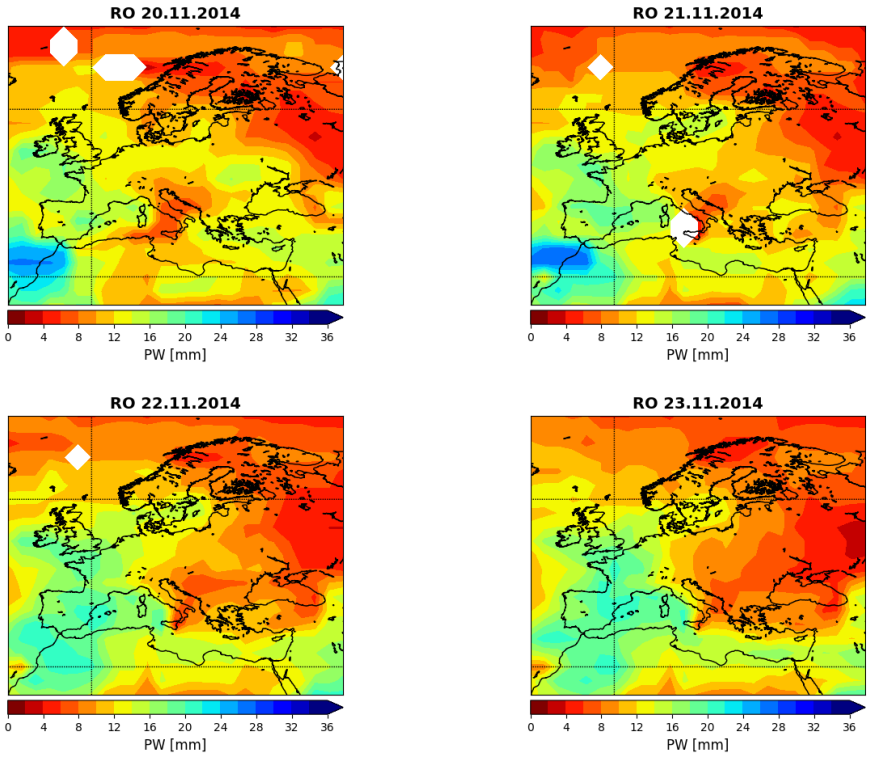

Figure 7.8.: *PW* 20th to 23rd of November 2014

7.5. General Remarks

Not all selected low-pressure systems can be seen equally well in the RO derived *PW* values. Especially when the event occurs within a period of increased *PW* values, the detection of comparatively small local low-pressure systems is quite difficult. A possible reason for this is explained in chapter 8.1. The visibility of the lows in the plots depends strongly on the chosen *PW* range. Especially for less pronounced events, choosing the right range is essential for detecting the low-pressure systems within these plots. While the event in 2009 can even be seen when using bigger ranges, the event of 2010 can hardly be seen within a smaller *PW* range. Deciding on the right range is a process of trial and error and there is probably no range that is ideal for all events, nevertheless to make it easier to compare the events to each other, the same range was applied to all events in this work.

8. Comparison to ECMWF reanalysis and forecast data

The events of 2009, 2010 and 2014 were also investigated in ECMWF reanalysis data. The event of 2014 was additionally analyzed with ECMWF forecast data. Figure 8.1 shows the *PW* plots for November the 7th as seen in the different data sets.

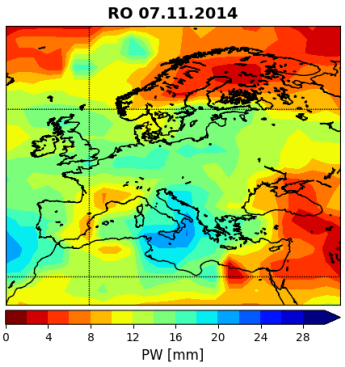

(a) RO

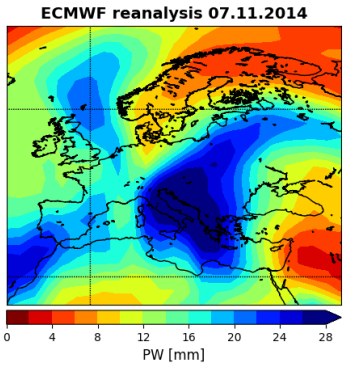

(b) ECMWF reanalysis

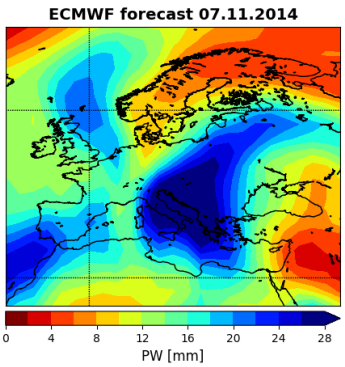

(c) ECMWF forecast

Figure 8.1.: Comparison of RO, ECMWF reanalysis and ECMWF forecast

These figures clearly show, that the *PW* values derived from the RO data are smaller than the ones in the ECMWF reanalysis (or forecast). These differences can be explained by the fact that RO measurements do not extend down to the Earth's surface, while the ECMWF data do. In this work the RO data usually

started at a pressure level of 950 hPa, in the case of data gaps sometimes at 800 hPa. This corresponds to an altitude of about 500-1500 m. Since 50% of the atmospheric water vapor is found in the lowest 2 km, the absence of humidity data from this altitudes leads to an underestimation of the *PW* value in the RO data. Figure 8.1 also shows, that the *PW* values calculated with the ECMWF reanalysis are nearly identical to the ones with the ECMWF forecast. This is not remarkable, since the ECMWF reanalysis uses the forecast for reanalyzing observations of the past.

8.1. Averaging

Before comparing the RO data to the ECMWF data, the ECMWF data had to be averaged. In figure 8.2 the *PW* plot of the averaged ECMWF reanalysis and of the non averaged ECMWF reanalysis are shown. Afterwards the averaged data are used for comparison plots.

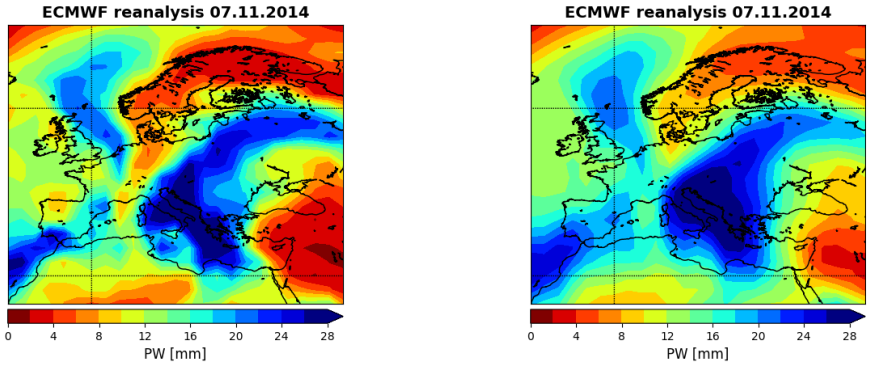

(a) non averaged **(b)** averaged

Figure 8.2.: *PW* of averaged and non averaged ECMWF reanalysis

As described in Brunner et al. (2016) the RO data were averaged with a Gaussian weighting function including ± 7.5° in longitude, ± 2.5° in latitude, and ± 2 days for each grid point. In order to make the ECMWF data comparable to these data, the ECMWF data had to be averaged as well. This averaging leads to a loss of small features in the *PW* plots, like e.g. a localized area of high *PW* values near Sicily in figure 8.2. This decrease in resolution poses a great problem in the detection of Mediterranean low-pressure systems. Especially the ± 7.5° in longitude, which correspond to roughly 800 km on the Earth's surface, lead to a smaller resolution than necessary for detecting lows with an average diameter that is way smaller than that. In addition the average lifetime of a Mediterranean cyclone is only 28h, which makes an averaging over ± 2 days for the posed question problematic.

8.2. March 2010

As described in 5.2, an Adriatic low-pressure system lead to heavy precipitation in the Mediterranean. In figure 8.3 the PW values for this event of the RO data (left side) and the ECMWF reanalysis data (right side) can be seen. This event was included because it shows the differences in visibility of lows between the RO data and the ECMWF reanalysis very well.

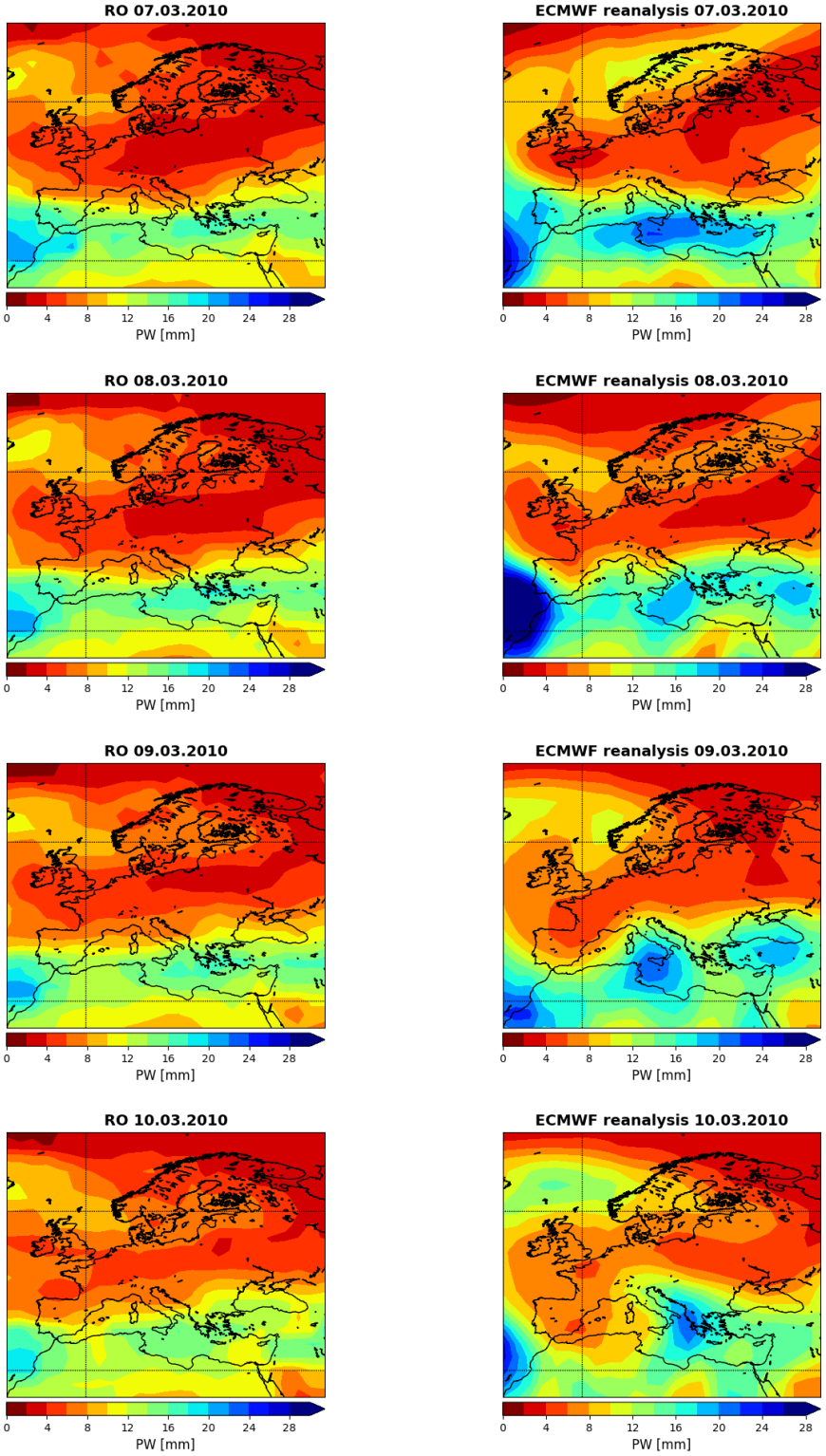

Figure 8.3.: *PW* values of the RO data (left side) and the ECMWF reanalysis data (right side)

Figure 8.3 illustrated the difference between the RO derived *PW* values and the ones derived from the ECMWF reanalysis. While the low-pressure system can't be seen in the RO data, it can be detected in the ECMWF data wherein the low is clearly visible on the 9th of March above the Mediterranean Sea. The system later moves over Sicily before it settles above the Adriatic, where it lead to snowfall in Italy and Croatia. Even though the low-pressure system can clearly be seen in the ECMWF reanalysis data, it cannot be seen on the day it actually occurred, but 2 days later. A delay in the occurrence of the lows in the RO/ECMWF data can be observed in all selected precipitation events, which can be traced back to the averaging of the data. Despite the strong averaging of ± 2 days, the longitudinal averaging of ±7.5° poses a bigger problem, since it smears out the results more than the averaging over time.

8.3. Absolute and Relative Difference

Figures 8.4 - 10.6 show the absolute and relative difference for one day (November the 7th) during the event in 2014. Figure 8.4 compares the RO data with the ECMWF reanalysis, figure 8.5 the RO data with the ECMWF forecast and figure 10.6 the ECMWF reanalysis with the ECMWF forecast.
The absolute and relative differences between the RO data and the ECMWF reanalysis data are very high (Fig. 8.4). The absolute difference above Central Europe lays at about -8 mm (or smaller), which means that the RO derived *PW* values are 8 mm smaller than the *PW* values of the ECMWF reanalysis, which corresponds to an underestimation of the event of about 60%. As mentioned before in chapter 8, this is due to the fact that RO measurements do not reach down to the Earth's surface but start at an altitude of about 1 km and therefore do not include a very moist part of the atmosphere. Even though the differences are in general very high, they are significantly smaller above Sicily, where the low-pressure system was located at the shown date. The accordance of the RO data with the ECMWF reanalysis/forecast is better at the grid points of the lows.
The differences between the RO data and the ECMWF forecast (Fig. 8.5) are very similar to the differences between the RO data and the ECMWF reanalysis. In comparison to the difference plots of the ECMWF reanalysis, some small features get smeared out and can therefore not be seen in the difference plots of the ECMWF forecast.
The comparison of the ECMWF reanalysis to the ECMWF forecast shows that the differences between these two data sets are very small. Since the ECMWF reanalysis also includes the ECMWF forecast, this was to be expected.

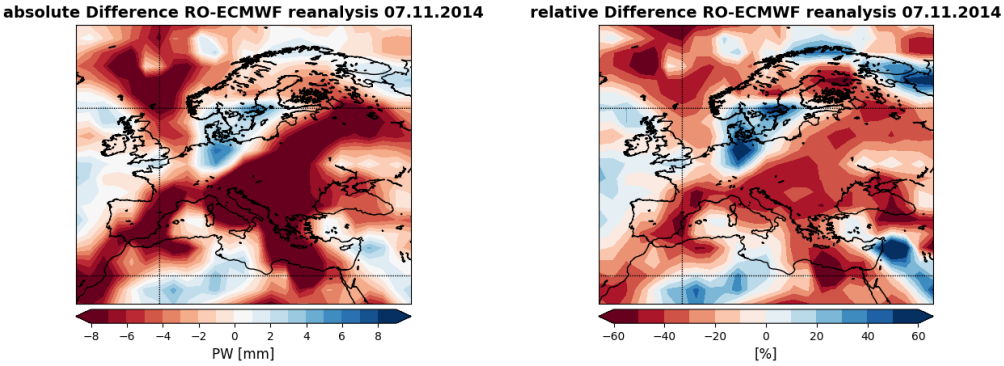

(a) absolute difference **(b)** relative difference

Figure 8.4.: Absolute and Relative Difference RO vs. ECMWF reanalysis

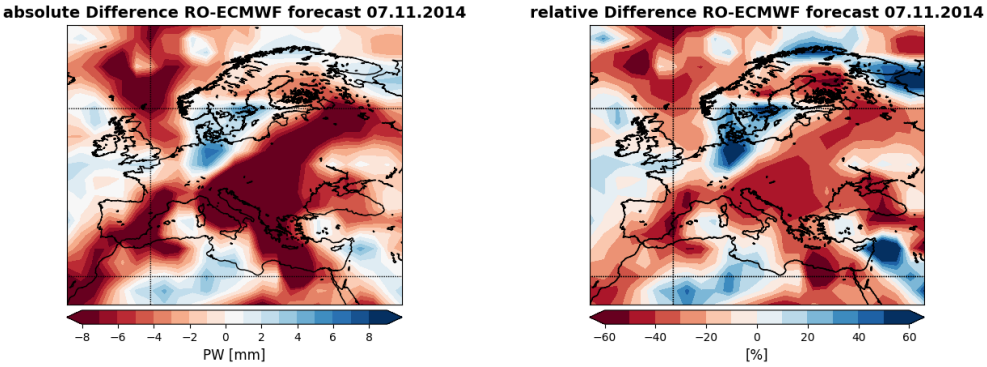

(a) absolute difference **(b)** relative difference

Figure 8.5.: Absolute and Relative Difference RO vs. ECMWF forecast

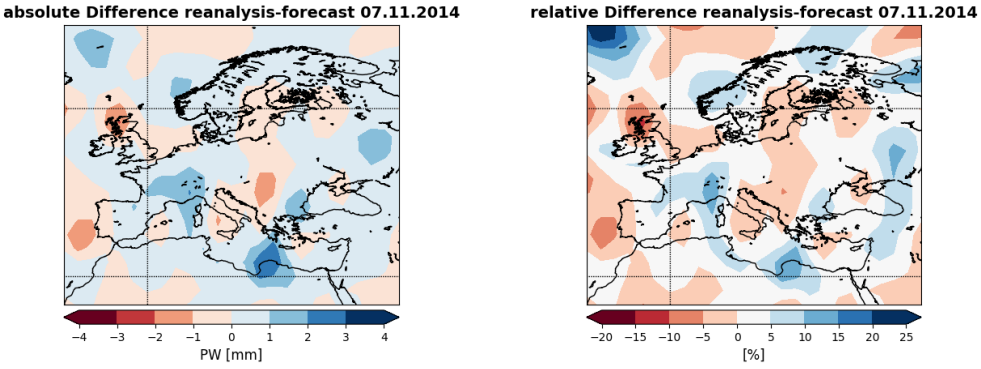

(a) absolute difference **(b)** relative difference

Figure 8.6.: Absolute and Relative Difference ECMWF reanalysis vs. ECMWF forecast

9. Tracks of the Low-Pressure Systems

To assess whether one can also see the path of the Mediterranean lows, the dates of the maxima in the PW values were investigated. For every event this was done once with the whole investigated period taken into account and with shorter time spans.

9.1. Event 2009

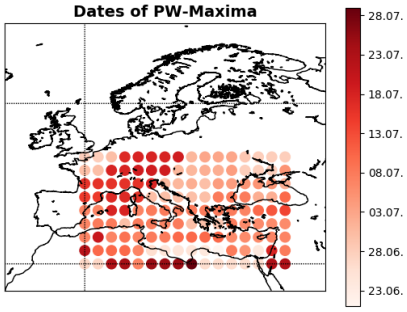

(a) whole period

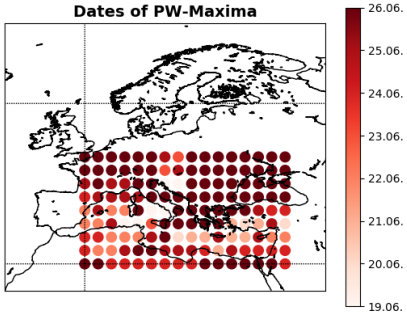

(b) 19.06.-26.06.

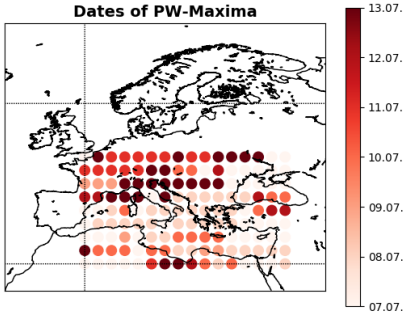

(c) 07.07.-13.07.

Figure 9.1.: Days of maximum PW value for each grid point

As seen in figure 9.1a, the maximum PW values occurred earlier in the east than in the west. Otherwise the occurrence dates of the maxima do not seem to

follow any pattern. As mentioned before, and shown by the plots in section 7.1, July 2009 was very wet in general. When taken the whole period from June 18th to July 31st into account, the maxima of the *PW* values therefore accumulate in late July. Tracing back the event in June (22nd-25th), with the whole period taken into account, is consequently not possible. For figure 9.1b a shorter time span (June 19th-26th) was chosen. The low-pressure system came from to east towards Austria, which can be seen in figure 9.1b (1st row, 6th-8th column). The maximum of the *PW* values was reached earlier in the easternmost grid point (June 23rd) than in the westernmost point (June 26th). Again a delay in the occurrence of the event, due to the averaging, is observed. As mentioned in 7.1, a low near Genoa can be seen in the *PW* plots around the 7th of June. Since the low-pressure system did not move far (only in the range of 2 grid points) and the surrounding grid points also showed quite high *PW* values around this time, figure 9.1c does not show a clear path of this low.

9.2. Event 2010

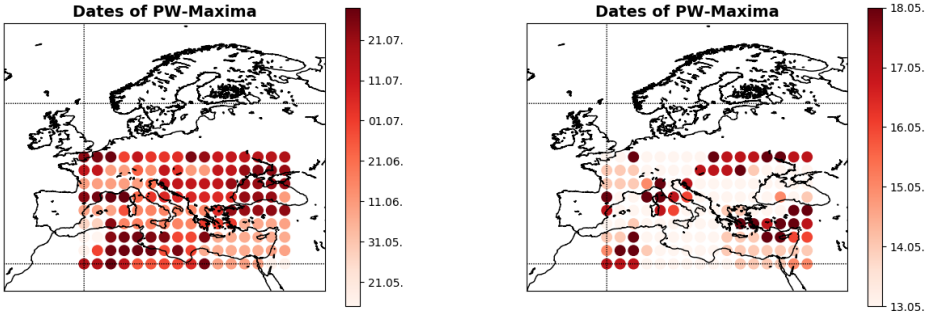

(a) whole period **(b)** 13.05.-18.05.

Figure 9.2.: Days of maximum *PW* value for each grid point

When using the whole period (May 1st to July 31st) for the calculation of the dates of the maximum *PW* values, no path can be seen (Figure 9.2a). Again the generally higher *PW* values in July lead to an accumulation of the occurrence of maxima at the end of the whole period and smaller events in May/June get lost. Figure 9.2b shows the maxima in the time between May 13th and May 18th. Most grid points experienced their maximum *PW* value at the 13th or 14th of May. Above Italy (7th column) 3 consecutive grid points show a path of a potential low-pressure system, which moved from the South northward but did not reach Austria, where the maximum *PW* values were reached at the 13th of May in this time span.

9.3. Event 2013

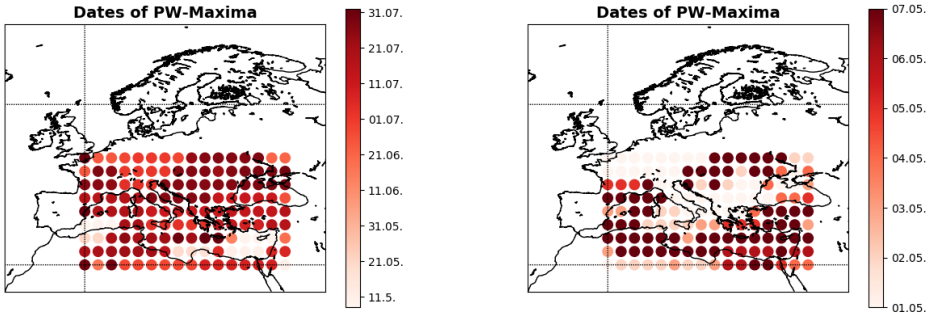

(a) whole period **(b)** 01.05.-07.05.

Figure 9.3.: Days of maximum *PW* value for each grid point

As described in 7.3, no low-pressure system could be clearly detected in the *PW* plots. Therefore, there is also no distinctive path visible in figure 9.3. Figure 9.3a again shows an accumulation of *PW* maxima in July and figure 9.3b only shows a path from the West to the East above the Mediterranean sea.

9.4. Event 2014

Figure 9.4a indicates once again, that taking too long time spans into account, makes retracing paths of low-pressure systems via the date of maximum *PW* value difficult. In figures 9.4b and 9.4c it can clearly be seen, that the highest *PW* values above Austria occurred at the beginning of November, however a clear path is not visible in the dates, unlike in figure 9.4d. Tracing the grid points above Italy, the maximum *PW* value is reached earlier in the South than in the North. While above Sicily the maximum is reached on November the 5^{th}, above Austria the *PW* value reached its peak around the 13^{th} of the month. This matches the path of the low-pressure system in the *PW* plots (7.7) quite well. Figure 9.4e shows the movement of the low from Austria to the East later in the month.

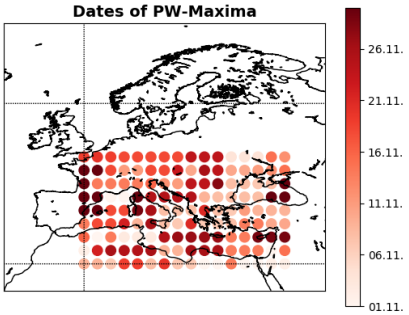

(a) whole period

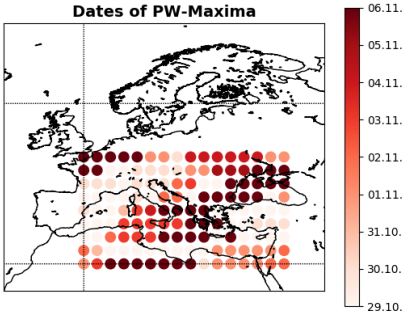

(b) 29.10.-06.11.

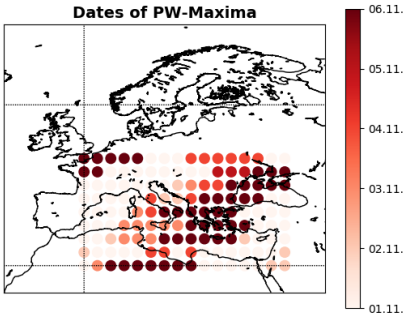

(c) 01.11.-06.11.

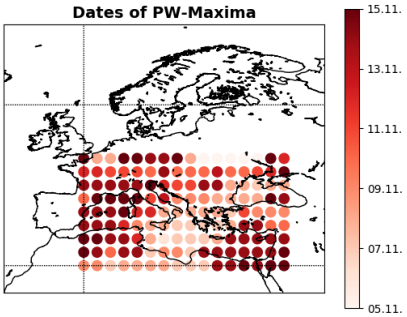

(d) 05.11.-15.11.

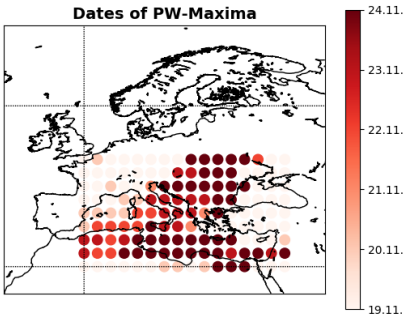

(e) 19.11.-24.11.

Figure 9.4.: Days of maximum PW value for each grid point

10. Vertical Structure

For the events in 2009, 2010 and 2014 the vertical distribution of the specific humidity was investigated. At first the specific humidity for four neighboring grid points was plotted and, since these profiles did not differ much from each other, afterwards averaged. Figure 10.1 shows the specific humidity of the RO data for November 2014 before they were averaged.

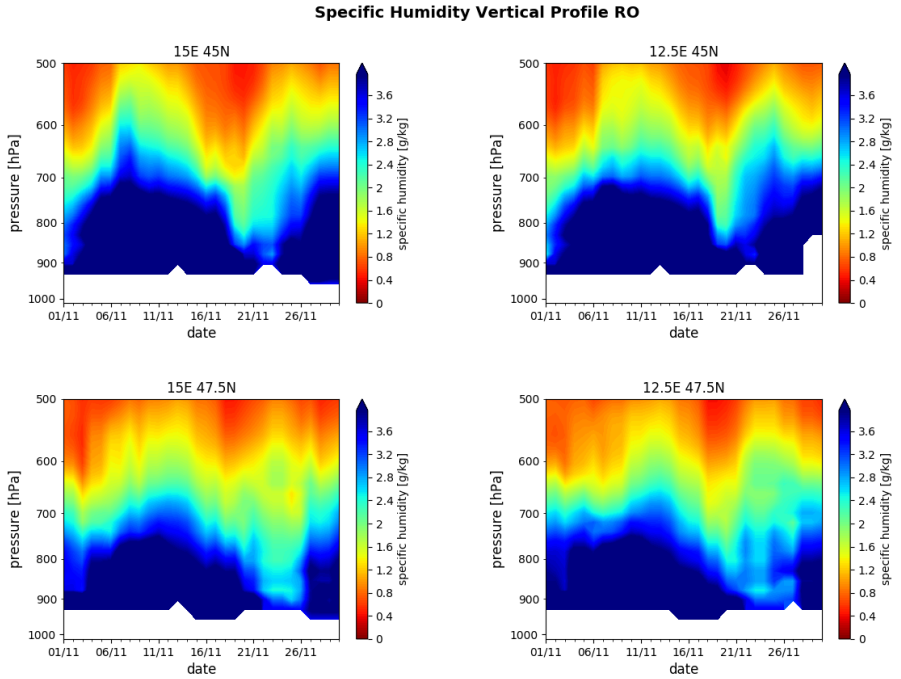

Figure 10.1.: Specific Humidity Vertical Structure for 4 grid points

The following figures are arranged as follows: In the upper left corner the vertical profile of the RO data is plotted, in the upper right corner the same for the ECMWF reanalysis data. In the lower left corner is the absolute difference between the upper plots and in the lower right corner the relative difference.

10.1. Event 2009

The specific humidity in figure 10.2 (both RO and ECMWF reanalysis) reveals, that the investigated time span was very wet in general. While the event that

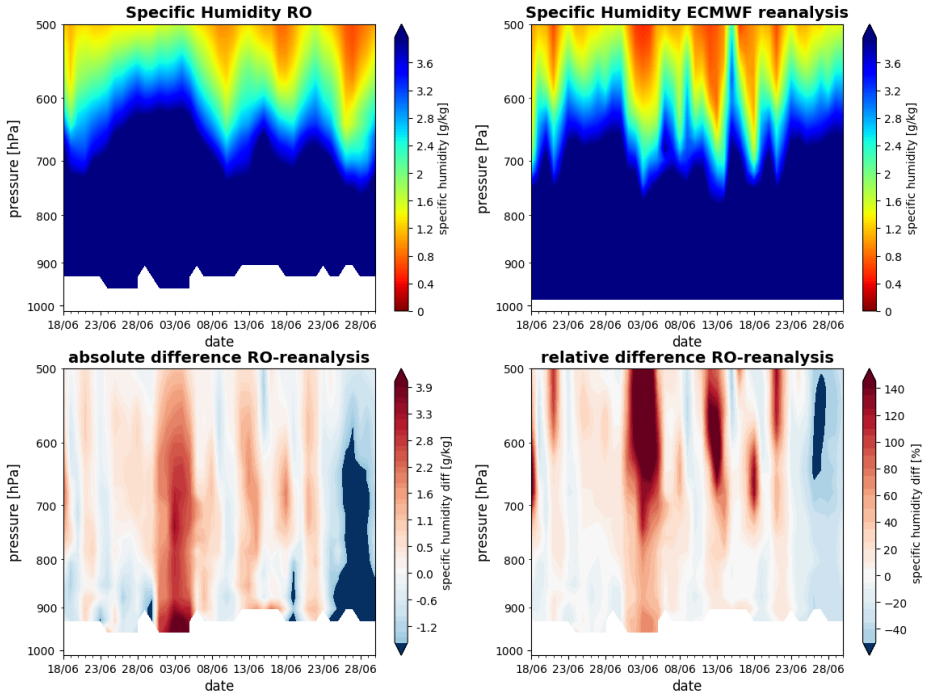

Figure 10.2.: Specific Humidity Vertical Structure: RO, ECMWF reanalysis, absolute and relative difference

occurred from the 22nd to the 25th of May can be seen in the RO data, the high specific humidity values persist until early June. Two less pronounced peaks are clearly visible in the RO data at the beginning of June. The ECMWF reanalysis data on the other side shows far more details than the RO data. The selected event is also visible in the ECMWF reanalysis data but again the increased specific humidity values persist longer than the actual event. Towards the end of the period an increase in the specific humidity values arises, which is completely missed in the RO data. This leads to comparatively huge values in the absolute and relative differences around the 28th of June. Otherwise, the difference plots show that the RO values in the troughs between the peaks are bigger than the ECMWF reanalysis values, which is due to the more detailed structure of the reanalysis data.

10.2. Event 2010

In March 2010 an Adriatic low-pressure system caused severe precipitation in Croatia and Italy. Since the *PW* plots of the RO data show no sign of such an event, they were compared to the ECMWF reanalysis data. Even though the

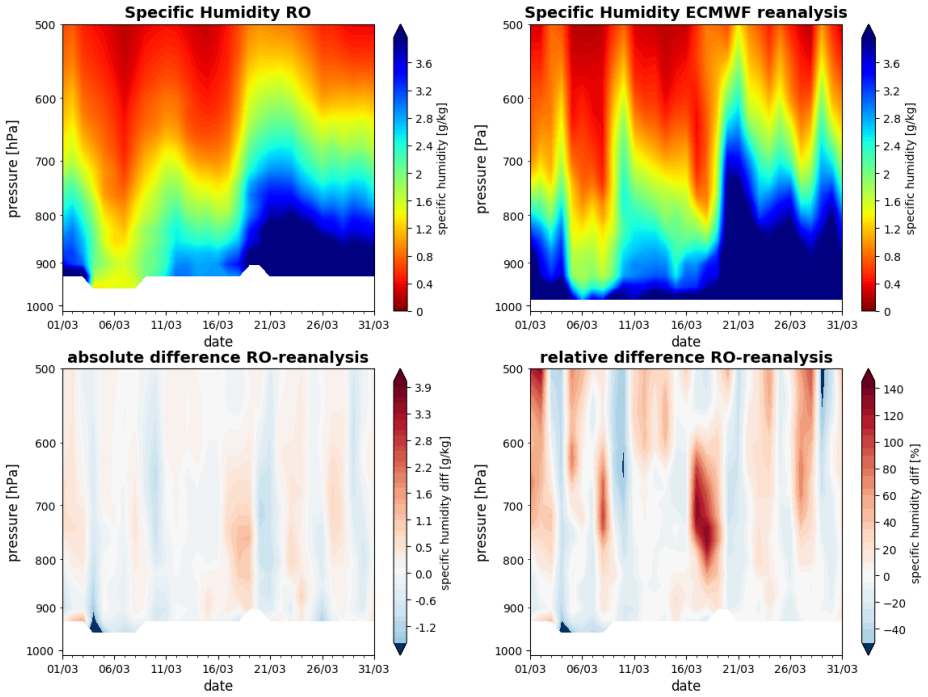

Figure 10.3.: Specific Humidity Vertical Structure: RO, ECMWF reanalysis, absolute and relative difference

low was originally predicted to reach Austria, it never actually got there, which can be seen in the specific humidity data. While the low-pressure system lead to heavy snowfall in Croatia around March the 7$^{\text{th}}$, the specific humidity values were especially low above Austria during this time. The abrupt increase in specific humidity around the 21$^{\text{st}}$ of the month is due to an Atlantic low, which moved across Central Europe. The accordance of the RO and the ECMWF reanalysis data seems to be better during dry periods, which leads to smaller differences than before.

10.3. Event 2014

In the case of the November 2014 event, the specific humidity data of the RO measurements exhibit far less structure than the ECMWF reanalysis data. The peaks around the 6$^{\text{th}}$ and the 21$^{\text{st}}$ of the month don't reach as high up in the atmosphere as the ECMWF data shows. In the ECMWF reanalysis data one can clearly see, that the precipitation was highest at the beginning of the month and slowly decreased until the 21$^{\text{st}}$ when a second peak occurred. The RO data shows the same chronological sequence but with far less detail. Due to the missing

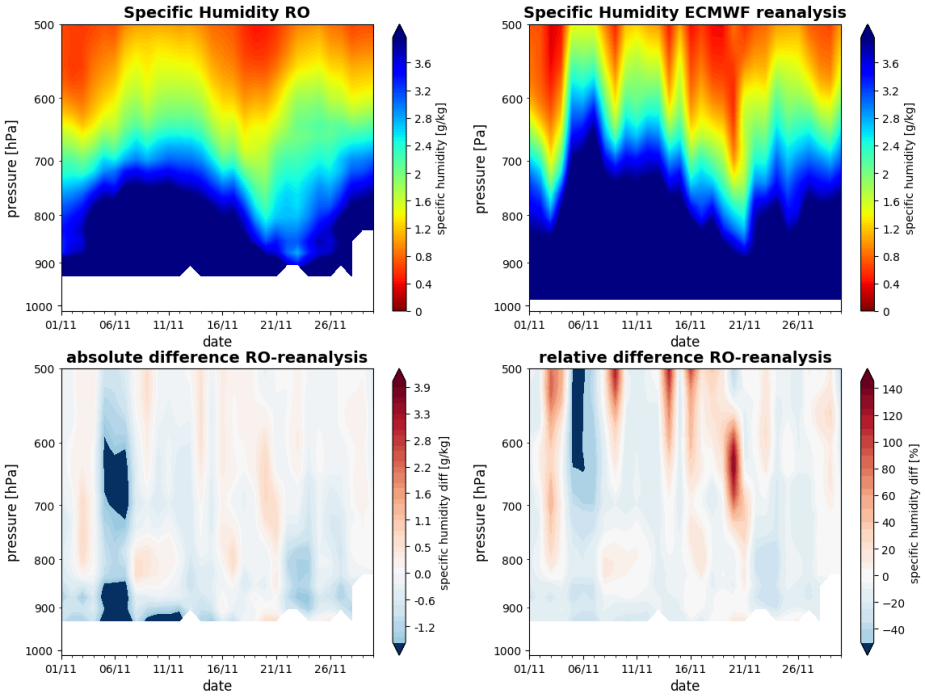

Figure 10.4.: Specific Humidity Vertical Structure: RO, ECMWF reanalysis, absolute and relative difference

surface-near data in the RO data, the differences are higher in the troughs before the 6th and the 21st of November.
For the event in 2014 the ECMWF forecast was also investigated. As expected, the ECMWF forecast leads to similar results as the ECMWF reanalysis but the data of the ECMWF forecast does not reach as far to the ground as the reanalysis. Nevertheless, the differences show nearly the same structure as before.

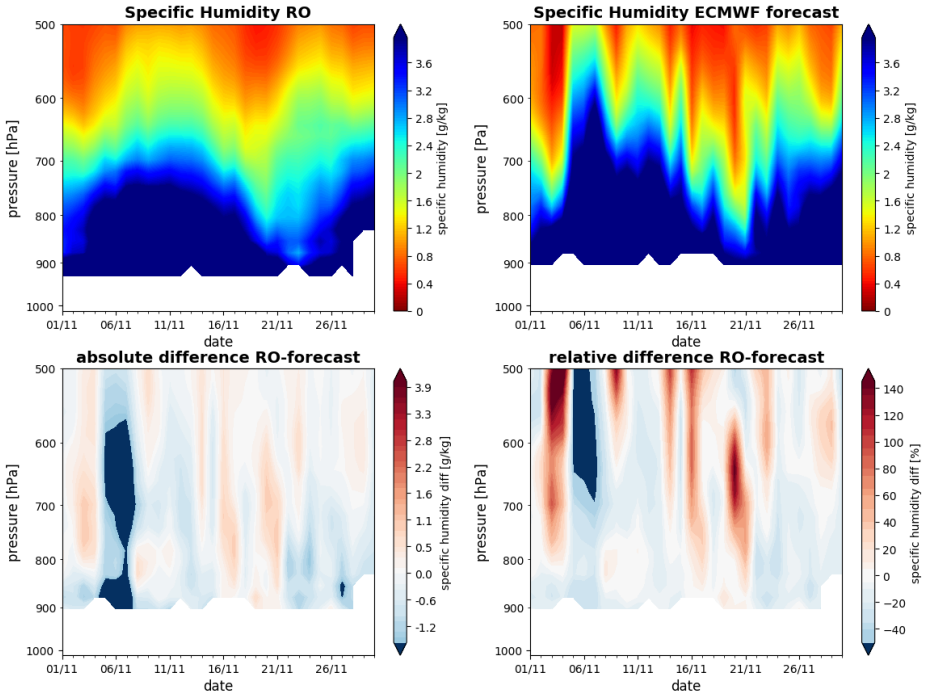

Figure 10.5.: Specific Humidity Vertical Structure: RO, ECMWF forecast, absolute and relative difference

For comparison reasons, the absolute and relative differences between the ECMWF reanalysis and the ECMWF forecast were also calculated (Figure 10.6). The comparison of the ECMWF forecast to the ECMWF reanalysis shows a high similarity, which leads to small differences between these two.

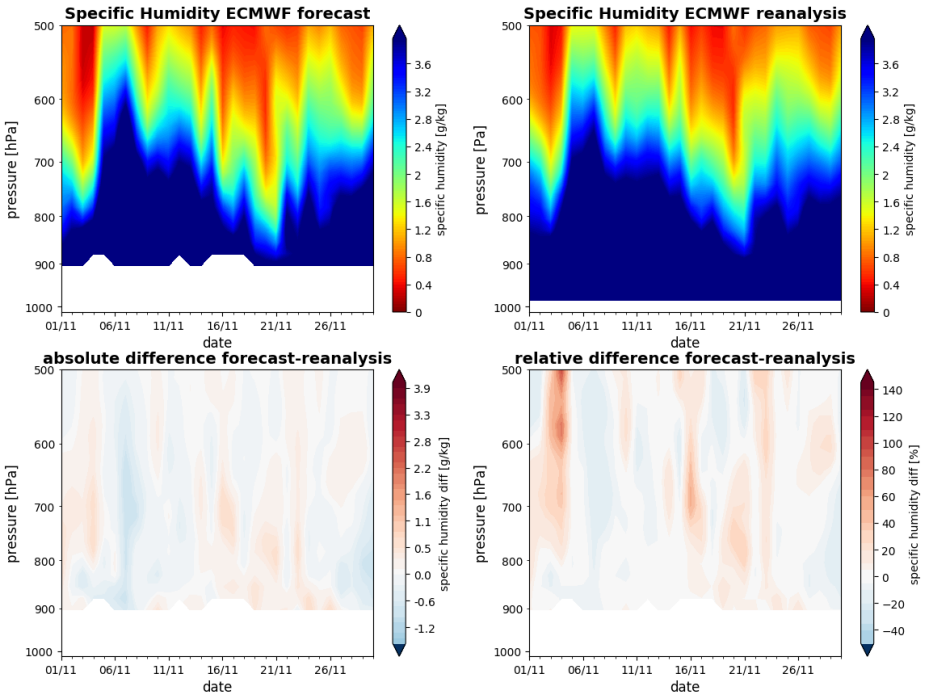

Figure 10.6.: Specific Humidity Vertical Structure: ECMWF forecast, ECMWF reanalysis, absolute and relative difference

11. Conclusions

The aim of this work was to assess whether Mediterranean low-pressure systems can be seen in RO derived humidity data. The events of 2009 and 2010 demonstrate that the visibility of Mediterranean low-pressure systems depends on how pronounced the investigated low is. Less distinctive systems, as in the case of the 2010 event, often are overshadowed by huge areas of high PW values and can therefore not be seen clearly in the RO derived humidity data. This also makes detecting Mediterranean lows in summer more difficult than in winter, since the amount of precipitation above Europe during summer is in general higher than in winter. Hence, the RO measurements of the event in November 2014 show the development and the path of the low-pressure system better than in the case of the other events, which all occurred in spring or summer. The visibilty also depends on the chosen range for the PW plots. As explained in section 7.5 this is especially important for less pronounced events. Comparison of the results of the RO measurements to weather maps of the Zentralanstalt für Meteorologie und Geodynamik (ZAMG) reveals major inconsistencies between the low-pressure systems that can be seen in the RO data and the ones detected by the ZAMG. A possible reason for those differences is the strong averaging of the RO measurements.

When compared to humidity data of the ECMWF reanalysis/forecast, the PW values of the RO derived data are considerably smaller than the ECMWF values. This is a result of the fact that RO measurements do not reach all the way down to the Earth's surface and therefore miss out on the wettest part of the atmosphere. The missing information of surface near regions has a huge impact on the RO derived PW values. As a result, precipitation events are less pronounced or missed completely in the RO derived data, such as the March 2010 event (section 8.2). However, the differences are smaller in the area of the low-pressure system, as already described in section 8.3. The biggest problem in this work was the strong averaging of the RO data. Due to the inclusion of $\pm$ 7.5° in longitude, $\pm$ 2.5° in latitude, and $\pm$ 2 days, the investigated events were less localized and appeared shifted in time in the RO derived data. The aim of this work was to assess, whether a detection of Mediterranean low-pressure systems in RO data is possible or not. Therefore already processed data were used, even though the averaging was not ideal for the exact detection and tracking of such localized lows. Nevertheless, more pronounced events could clearly be seen in the averaged RO data, which makes it an interesting and promising topic for future studies.

Under the assumption that the PW values are highest in the center of the low-pressure system, one can trace the path of lows via the date of maximum PW value in each grid point. This is a quick and easy method to visualize the rough path of a low-pressure system. However, the paths are only visible if the low is pronounced enough and moved over more than only a few grid points. The chosen time span for the calculations should not be too long, since generally wetter periods overshadow low-pressure systems and make detecting the path of such a low with this simple method impossible. Despite the possibility of tracking lows, the investigation of the dates of maximum PW values also shows accumulations of these maxima in certain periods, e.g., in summer. As mentioned before, retracing the paths of low-pressure systems is more difficult, when the amount of precipitable water is generally higher, therefore this method worked best for the November 2014 event, which is the only investigated event in this work which did not occur in spring/summer. Despite its simplicity, retracing the paths of low-pressure systems via the dates of maximum PW values, can give additional information about lows and the time periods they occur in.

The vertical structure of the specific humidity once again showed, that the ECMWF reanalysis and forecast data have a more pronounced structure than the RO data. The lack of surface-near information in the RO data leads to a loss in detail in the vertical structure, where the events do not seem to reach as high up in the atmosphere as in the ECMWF data. The differences between the data sets are therefore higher between the peaks that get lost in the RO data. A height from which on the RO data took the lead could not be seen in the used data sets. As suspected, the ECMWF forecast lead to very similar results as the ECMWF reanalysis, despite the lack of surface-near data in the forecast.

To sum up, detecting Mediterranean low-pressure systems in radio occultation derived humidity data is a fast and easy way to get an idea of the rough path and the extension of such a system. Since the shown method is based on visual detection of lows in RO derived precipitable water values, it works better for precipitation events in autumn and winter when the general amount of precipitation above Europe is lower. Strong averaging and the lack of surface-near measurements in the RO data, caused the events to appear less pronounced, less detailed, and shifted in time. Even though the averaging of the used RO data posed a problem, nearly all selected events could be detected in the data. The maxima of the PW values can be used to roughly retrace the track of a low-pressure system without much effort by investigating the dates of the highest PW values. Choosing the right time span is essential for this method, since generally wetter periods overshadow low-pressure systems with an average lifespan of 28h easily. The comparison of the RO data to the ECMWF data showed that under these preconditions using RO data yields no advantages in detecting Mediterranean low-pressure systems above the ECMWF reanalysis data. Nevertheless, it can be used as an ancillary source of information for already established methods in detecting low-pressure systems.

List of Figures

Bibliography

American Meteorological Society (2012). *AMS Glossary - Triple State*. last accessed: 20-11-2019. URL: http://glossary.ametsoc.org/wiki/Triple_state.

Atmospheric Research, UCAR - University Corporation for (2019a). *Global Navigation Satellite System Radio Occultation (GNSS-RO)*. last accessed: 13-11-2019. URL: https://www.cosmic.ucar.edu/what-we-do/gnss-radio-occultation/.

– (2019b). *The Troposphere - overview*. last accessed: 07-10-2019. URL: https://scied.ucar.edu/shortcontent/troposphere-overview.

Brönnimann, S. (2018). *Klimatologie*. German. utb.

Brunner, L. (July 2014). "Stratospheric ozone and temperature evolution over the past decades". MA thesis. Wegener Center for Climate and Global Change, University of Graz. DOI: 10.13140/RG.2.2.16933.29922.

Brunner, L., A. K. Steiner, B. Scherllin-Pirscher, and M. W. Jury (2016). "Exploring atmospheric blocking with GPS radio occultation observations". *Atmospheric Chemistry and Physics* 16.7, pp. 4593–4604. DOI: 10.5194/acp-16-4593-2016. URL: https://www.atmos-chem-phys.net/16/4593/2016/.

Campbell, M. K. and S. O. Farrell (2009). *Biochemistry, Sixth Edition*. Thomson Brooks/Cole.

Danish Meteorological Institute (2019). *EUMETSAT ROM SAF Radio Occultation Meteorology*. last accessed: 28-09-2019. URL: http://www.romsaf.org/.

Danzer, J., B. Scherllin-Pirscher, and U. Foelsche (2013). "Systematic residual ionospheric errors in radio occultation data and a potential way to minimize them". *Atmospheric Measurement Techniques* 6.8, pp. 2169–2179. DOI: 10.5194/amt-6-2169-2013. URL: https://www.atmos-meas-tech.net/6/2169/2013/.

Deutscher Wetterdienst (2019). *Deutscher Wetterdienst, Vb-Wetterlage*. last accessed: 17-10-2019. URL: https://www.dwd.de/DE/service/lexikon/Functions/glossar.html?lv2=102868&lv3=102888.

Dowling, T. E. and A. P. Showman (2007). *Encyclopedia of the Solar System (Second Edition): Earth as a Planet - Atmosphere and Oceans*. Elsevier.

ECMWF (2019a). *ECMWF/Research/Climate reanalysis*. last accessed: 22-11-2019. URL: https://www.ecmwf.int/en/research/climate-reanalysis.

– (2019b). *ECMWF/Research/Data assimilation*. last accessed: 22-11-2019. URL: https://www.ecmwf.int/en/research/data-assimilation.

– (2019c). *ECMWF/Research/Modelling and prediction*. last accessed: 30-10-2019. URL: https://www.ecmwf.int/en/research/modelling-and-prediction.

Elmhurst College - Charles E.Ophardt (2003). *Virtual Chembook*. last accessed: 09-10-2019. URL: http://chemistry.elmhurst.edu/vchembook/206bent.html.

Encyclopædia Britannica (2016a). *Encyclopædia Britannica - Cyclogenesis*. last accessed: 17-10-2019. URL: https://www.britannica.com/science/cyclogenesis.

– (2016b). *Encyclopædia Britannica - Cyclone*. last accessed: 16-10-2019. URL: https://www.britannica.com/science/cyclone-meteorology.

Engineering ToolBox (2003). *Engineering ToolBox, Air - Composition and Molecular Weight*. last accessed: 17-01-2020. URL: https://www.engineeringtoolbox.com/air-composition-d_212.htmll.

EODC (2019). *Earth Observation Data Centre for Water Resources Monitoring GmbH*. last accessed: 28-09-2019. URL: https://www.eodc.eu/.

Feltz, M., R. Knuteson, S. Ackerman, and H. Revercomb (2014). "Application of GPS radio occultation to the assessment of temperature profile retrievals from microwave and infrared sounders". *Atmospheric Measurement Techniques* 7, pp. 3751–3762. DOI: 10.5194/amt-7-3751-2014.

Foelsche, U., A. Gobiet, A. K. Steiner, M. Borsche, J. Wickert, T. Schmidt, and G. Kirchengast (2006). "Global Climatologies Based on Radio Occultation Data: The CHAMPCLIM Project". In: *Atmosphere and Climate Studies by Occultation Methods*. Springer.

Fu, E., K.i Zhang, F. Wu, X.a Xu, K. Marion, A. Rea, Y. Kuleshov, and G. Weymouth (June 2007). "An Evaluation of GNSS Radio Occultation Technology for Australian Meteorology". *Journal of Global Positioning Systems* 6, pp. 74–79. DOI: 10.5081/jgps.6.1.74.

GFZ (2008). *Helmholtz Centre Potsdam German Research Centre for Geosciences - GFZ*. last accessed: 13-11-2019. URL: http://www-app2.gfz-potsdam.de/pb1/GASP/GASP2/GRACE/index_grace.html.

– (2019). *Helmholtz Centre Potsdam German Research Centre for Geosciences - GFZ*. last accessed: 13-11-2019. URL: https://www.gfz-potsdam.de/sektion/geodaetische-weltraumverfahren/projekte/champ-ro/.

Haiden, T. (June 2009). *Meteorologische Analyse des Niederschlags von 22.-25. Juni 2009*. Zentralanstalt für Meteorologie und Geodynamik. German.

Hajj, G., R. Kursinski, L.J. Romans, W.I. Bertiger, and S. Leroy (2002). "A Technical Description of Atmospheric Sounding by GPS Occultation". *Journal of Atmospheric and Solar-Terrestrial Physics* 64, pp. 451–469. DOI: 10.1016/S1364-6826(01)00114-6.

HyMeX (2019). *HyMeX – Hydrological cycle in the Mediterranean Experiment 2010-2020*. last accessed: 26-11-2019. URL: https://www.hymex.org/?page=news.

Jin, S., E. Cardellach, and F. Xie (2014). *GNSS Remote Sensing - Theory, Methods and Applications*. Springer.

Kaidor (2013). *Global circulation of Earth's atmosphere displaying Hadley cell, Ferrell cell and polar cell*. last accessed: 17-10-2019. URL: https://en.wikipedia.org/wiki/Atmospheric_circulation#/media/File:Earth_Global_Circulation_-_en.svg.

Kertz, W. (1971). *Einführung in die Geophysik II*. German. Bibliographisches Institut AG.

Kursinski, E. R., G. A. Hajj, J. T. Schofield, R. P. Linfield, and K. R. Hardy (1997). "Observing

Global Positioning System". *Journal of Geophysical Research: Atmospheres* 102.D19, pp. 23429–23465. DOI: 10.1029/97JD01569. URL: https://agupubs.onlinelibrary.wiley.com/doi/abs/10.1029/97JD01569.

Löscher, A. and G. Kirchengast (2006). "Assimilation of GNSS Radio Occultation Profiles into GCM Fields for Global Climate Analysis". In: *Atmosphere and Climate Studies by Occultation Methods*. Springer.

McGraw-Hill (1984). *Concise Encyclopedia of Science and Technology*. McGraw-Hill Education Ltd.

Midwestern Regional Climate Center (2016). *Living with weather*. last accessed: 15-10-2019. URL: https://mrcc.illinois.edu/living_wx/winds/index.html.

NASA (2013). *Geometric altitude vs. temperature, pressure, density, and the speed of sound derived from the 1962 U.S. Standard Atmosphere*. last accessed: 29-10-2019. URL: http://www.centennialofflight.net/essay/Theories_of_Flight/atmosphere/TH1G1.htm.

National Oceanic and Atmospheric Administration (2019). *Greenhouse Gases*. last accessed: 10-10-2019. URL: https://www.ncdc.noaa.gov/monitoring-references/faq/greenhouse-gases.php#h2o.

NOAA (2019). *GPS.gov - National Oceanic and Atmospheric Administration*. last accessed: 25-09-2019. URL: https://www.gps.gov/.

Poli, P. (2006). "Assimilation of GNSS Radio Occultation Data into Numerical Weather Prediction". In: *Atmosphere and Climate Studies by Occultation Methods*. Springer.

Rieckh, T. (2018). "Investigating the value of GPS radio occultation water vapor data using in-situ and remote sensing techniques and models". PhD thesis. Wegener Center for Climate and Global Change, University of Graz.

Rieckh, T., R. Anthes, W. Randel, S. Ho, and U. Foelsche (Mar. 2017). "Tropospheric dry layers in the tropical western Pacific: Comparisons of GPS radio occultation with multiple data sets". *Atmospheric Measurement Techniques* 10, pp. 1093–1110. DOI: 10.5194/amt-10-1093-2017.

Roedel, W. (1994). *Physik unserer Umwelt - Die Atmosphäre*. German. Springer Verlag.

Smith, E. K. and S. Weintraub (1953). "The Constants in the Equation for Atmospheric Refractive Index at Radio Frequencies". *Proceedings of the IRE* 41.8, pp. 1035–1037. ISSN: 2162-6634. DOI: 10.1109/JRPROC.1953.274297.

Stevens, B. and S. Bony (2013). "Water in the Atmosphere". *Physics Today* 66, pp. 29–34. DOI: 10.1063/PT.3.20090.

Trigo, I. F., T. D. Davies, and G. R. Bigg (1999). "Objective Climatology of Cyclones in the Mediterranean Region". *Journal of Climate* 12.6, pp. 1685–1696. DOI: 10.1175/1520-0442(1999)012<1685:OCOCIT>2.0.CO;2. URL: https://doi.org/10.1175/1520-0442(1999)012%3C1685:OCOCIT%3E2.0.CO;2.

Woods, A. (2005). *Medium-Range Weather Prediction*. Springer.

ZAMG (2010). *Zentralanstalt für Meteorologie und Geodynamik - ZAMG*. last accessed: 16-11-2019. URL: https://www.zamg.ac.at/fix/klima/wiewars05-10.pdf.

ZAMG (2013a). *Zentralanstalt für Meteorologie und Geodynamik - ZAMG*. last accessed: 22-11-2019. URL: https://www.zamg.ac.at/cms/de/klima/news/update-starkregen-und-rueckblick-mai.

– (2013b). *Zentralanstalt für Meteorologie und Geodynamik - ZAMG*. last accessed: 22-11-2019. URL: https://www.zamg.ac.at/cms/de/klima/news/juni-2013-nass-und-trocken-kuehl-und-heiss.

– (2014a). *Zentralanstalt für Meteorologie und Geodynamik - ZAMG*. last accessed: 30-10-2019. URL: https://www.zamg.ac.at/cms/de/wetter/news/teils-extreme-regenmengen-in-osttirol-und-oberkaernten.

– (2014b). *Zentralanstalt für Meteorologie und Geodynamik - ZAMG*. last accessed: 30-10-2019. URL: https://www.zamg.ac.at/cms/de/klima/news/waermster-november-seit-messbeginn.

– (2019a). *Zentralanstalt für Meteorologie und Geodynamik - ZAMG*. last accessed: 15-11-2019. URL: https://www.zamg.ac.at/cms/de/wetter/wetterkarte.

– (2019b). *Zentralanstalt für Meteorologie und Geodynamik - ZAMG*. last accessed: 22-11-2019. URL: https://www.zamg.ac.at/cms/de/klima/klima-aktuell/klimamonitoring/?param=rr&period=period-ym-2010-05&ref=3.

Zeit (2010). *Schneechaos in Italien, Kroatien und Spanien*. last accessed: 15-11-2019. URL: https://web.archive.org/web/20100313132916/http://www.zeit.de/newsticker/2010/3/10/iptc-bdt-20100310-115-24169076xml.

Eidestattliche Erklärung

Hiermit erkläre ich, dass ich die vorliegende Arbeit selbständig angefertigt habe und keine anderen als die angeführten Hilfsmittel benutzt habe. Im Wortlaut oder wesentlichen Inhalt übernommene Formulierungen aus (un)gedruckten Quellen wurden entsprechend gekennzeichnet und mit genauer Quellenangabe versehen.

Graz, am 27.01.2020

Stephanie Haas BSc